

A Novel 3D Non-Stationary Maritime Wireless Channel Model

Yubei He[✉], Cheng-Xiang Wang[✉], *Fellow, IEEE*, Hengtai Chang[✉], Jie Huang[✉], *Member, IEEE*,
 Jian Sun[✉], *Member, IEEE*, Wensheng Zhang[✉], *Member, IEEE*,
 and El-Hadi M. Aggoune[✉], *Life Senior Member, IEEE*

Abstract—In this paper, a novel 3-dimensional (3D) non-stationary geometry-based stochastic model (GBSM) is proposed to mimic the ship-to-ship multiple-input multiple-output (MIMO) communication channels. To reflect the realistic maritime propagation environment, the effects of rough sea surface scattering and evaporation duct propagation are investigated in the proposed channel model. The model considers the movements of transmitter (Tx), receiver (Rx), and scatterers, and

is capable of capturing the channel characteristics, including non-stationary characteristics, spatial consistency, location-dependent property, etc. Through taking the array cluster evolution into account, the proposed channel model can describe massive MIMO channels and can easily switch to conventional MIMO channel model by adjusting corresponding parameters. Based on the proposed model, key statistical properties like delay/angular/Doppler power spectrum density (PSD), space-time correlation function (STCF), stationary interval, and root mean square (RMS) Doppler/delay spreads in multi-scenarios are derived. The usefulness and accuracy of the proposed model are demonstrated by comparing theoretical results, simulation results, and corresponding measurement results.

Index Terms—Maritime ship-to-ship communications, 3D non-stationary wireless channel, GBSM, statistical characteristics.

I. INTRODUCTION

OVER the past few years, the sustained and rapid development of maritime economy raises greater demands on the performance of maritime communication technologies. The traditional fishing and transportation, as well as the emerging tourism require more efficient maritime wireless communication systems with high data transmission rate and low latency [1], [2]. The maritime communication is an essential part of the space-air-ground-sea integrated network and plays an important role in expanding global communications coverage for future sixth generation (6G) wireless communication networks [3], [4]. Therefore, the design of reliable communication systems and the innovation of technologies in maritime communication have drawn growing attention from researchers. To optimize system performance and improve algorithm design [5], it is critical to understand the wireless propagation characteristics of maritime channel arising from the uniqueness of the maritime environment. Unlike the well-studied terrestrial communication channel, there is still a lack of related work in maritime channel characteristic analysis and channel modeling. Therefore, it is urgent to establish practical maritime channel models.

Up to now, some channel measurement campaigns have been performed to investigate the maritime channel properties, and some empirical channel models have been obtained based on the channel measurements results. In [6]–[8], the channel measurement campaigns at 5.2 GHz for ship-to-ship and ship-to-land scenarios were conducted to study the large-scale fading and small-scale fading characteristics, and the scattering phenomenon caused by the roughness of the sea surface.

Manuscript received April 3, 2021; revised October 16, 2021; accepted November 17, 2021. Date of publication December 10, 2021; date of current version March 17, 2022. This work was supported in part by the National Key Research and Development Program of China under Grant 2018YFB1801101; in part by the National Natural Science Foundation of China (NSFC) under Grant 61960206006, Grant 61771293, Grant 61901109, and Grant 62071276; in part by the Frontiers Science Center for Mobile Information Communication and Security; in part by the High Level Innovation and Entrepreneurial Research Team Program in Jiangsu; in part by the High Level Innovation and Entrepreneurial Talent Introduction Program in Jiangsu; in part by the Research Fund of National Mobile Communications Research Laboratory, Southeast University, under Grant 2020B01; in part by the Fundamental Research Funds for the Central Universities under Grant 2242021R30001; in part by the EU H2020 RISE TESTBED2 Project under Grant 872172; in part by the Taishan Scholar Program of Shandong Province; in part by the Shandong Natural Science Foundation under Grant ZR2019BF040 and Grant ZR2020MF002; in part by the Open Research Fund of Key Laboratory of Dynamic Cognitive System of Electromagnetic Spectrum Space, Ministry of Industry and Information Technology, under Grant KF20202108; in part by the Fundamental Research Funds of Shandong University under Grant 2020GN032; and in part by SNCS at the University of Tabuk, Saudi Arabia under Grant 002/1442H. The associate editor coordinating the review of this article and approving it for publication was E. Björnson. (*Corresponding authors: Cheng-Xiang Wang; Jian Sun.*)

Yubei He and Wensheng Zhang are with the Shandong Provincial Key Laboratory of Wireless Communication Technologies, School of Information Science and Engineering, Shandong University, Qingdao 266237, China (e-mail: heyubei@126.com; zhangwsh@sdu.edu.cn).

Cheng-Xiang Wang and Jie Huang are with the National Mobile Communications Research Laboratory, School of Information Science and Engineering, Southeast University, Nanjing 210096, China, and also with Purple Mountain Laboratories, Nanjing 211111, China (e-mail: chxwang@seu.edu.cn; j_huang@seu.edu.cn).

Hengtai Chang is with Purple Mountain Laboratories, Nanjing 211111, China (e-mail: changhengtai@pmlabs.com.cn).

Jian Sun is with the Shandong Provincial Key Laboratory of Wireless Communication Technologies, School of Information Science and Engineering, Shandong University, Qingdao 266237, China, and also with the Key Laboratory of Dynamic Cognitive System of Electromagnetic Spectrum Space, Ministry of Industry and Information Technology, Nanjing University of Aeronautics and Astronautics, Nanjing, Jiangsu 211106, China (e-mail: sunjian@sdu.edu.cn).

El-Hadi M. Aggoune is with the Sensor Networks and Cellular Systems Research Center, University of Tabuk, Tabuk 47315, Saudi Arabia (e-mail: haggoune.snrc@ut.edu.sa).

Color versions of one or more figures in this article are available at <https://doi.org/10.1109/TCOMM.2021.3134275>.

Digital Object Identifier 10.1109/TCOMM.2021.3134275

At 5.8 GHz, a lot of channel measurement campaigns were carried out in sea port environment [9]–[11]. In [9], [10], the authors used buoys at different positions to measure the changes of received signal level and time dispersion parameters with line-of-sight (LoS) and non-LoS (NLoS) propagation. In [11], the effect of antenna height on signal attenuation was investigated, and the two-ray model was used to fit the measured path loss results. In [12], the statistical properties such as power delay profile (PDP), mean excess delay, and root mean square (RMS) delay spread were obtained from the measurement of 4×4 multiple-input multiple-output (MIMO) communication links at 2.4 GHz. By analyzing the received signal strength, it was found that the scattering rays from the rough sea surface could not be ignored, and a distance-based path loss model was developed. The measurement results of [13] showed that the channel performance could be improved considerably after using diversity scheme, especially in NLoS scenario. In [14], [15], the channel was measured at 2 GHz with short distance (15.5 km) and long distance (45 km) to study the channel characteristics and the coverage for different kinds of antennas. According to the measurement results in [16], the beyond-LoS (B-LoS) communications can be achieved by using evaporation duct transmission over hundreds of kilometers distance. By conducting a long-distance measurement campaign at 5 GHz [17], [18], the predictive ability of the two-ray path loss model was found to deteriorate when the transmission distance became large, while the three-ray model with an additional refraction path caused by evaporation duct can better match the measurement data. This phenomenon indicated that disregarding duct effect may lead to inaccurate results. However, the related works mainly focused on the study of large-scale fading, and there is still a lack of research on the influence of duct effect on small-scale channel characteristics. Although the empirical models are practically significant, the measurement campaigns are time consuming and the corresponding models are susceptible to specific environments and limited by fixed experimental setup.

Other channel models used in maritime channel characterization mainly include deterministic models and stochastic models. For deterministic models, the main methods are ray-tracing and finite-difference time domain (FDTD) methods. Both [19] and [20] adopted ray-tracing method at 35 GHz and 94 GHz to study the difference of the channel characteristics at millimeter wave (mmWave) frequency band and other frequency bands. Nevertheless, the sea surface was assumed to be flat and the movement of transceiver was not considered in the simulation, because ray-tracing method is not adaptable to changing scenarios. In [21], [22], depending on the simulated random sea surface, the scattering multipath components (MPCs) were studied by using FDTD method. Due to the difficulty in the design of boundary conditions, the effect of evaporation duct was not explored in the aforementioned FDTD simulation. In addition, the authors of [23], [24] combined the empirical model and the deterministic model to describe the path loss in signal propagation, but did not conduct studies on small-scale fading. From what has been discussed above, the deterministic channel modeling methods can accurately simulate the propagation process of radio

waves, but they are not flexible and time-variant because of huge calculation complexity and high dependency on specific scenario settings. The stochastic models can be further divided into geometry-based stochastic models (GBSMs) and non-geometry-based stochastic models (NGSMs). In [25], [26], the two-ring model was used to describe the distribution of the scatterers around the ships, and the statistical properties such as temporal autocorrelation functions (ACFs) and spatial cross-correlation functions (CCFs) were calculated. However, the models were 2-dimensional (2D) and ignored the variation of the maritime environment. In [27], the conventional two-ray model was improved by superimposing a Gaussian random variable to introduce the description of channel randomness. Nevertheless, most of the existing stochastic models do not adequately consider the fluctuation of sea surface and the resulting 3-dimensional (3D) motion of antennas.

Based on the research results of the current experiments and modeling, the distinctive channel characteristics caused by the uniqueness of maritime environment include:

- a) The rough sea surface will result in the scattering of signal. Besides, the sea surface is not static, and the time-variant sea waves will introduce randomness in the maritime communication channel.
- b) Due to the variation of water vapour pressure and temperature with height, the gradient of refractivity in marine atmosphere appears in the first tens of meters above sea surface, and the evaporation duct is formed. By trapping the electromagnetic wave, the evaporation duct can support the communications over the horizon.
- c) There is location-dependent property in the maritime channel [1]. Depending on the distance between transmitter (Tx) and receiver (Rx), the MPCs generated by sea wave scattering, evaporation duct propagation, and LoS propagation will appear or disappear in the channel.
- d) Because of the fluctuation of sea waves, the antennas mounted on the ships will experience 3D movements, which will cause the non-stationary characteristic and Doppler frequency shift of channel.

In order to mimic the impact of maritime environment on communications accurately, the channel model should consider all the characteristics presented above. However, to the best of our knowledge, the existing models cannot reflect the location-dependent property and time non-stationary characteristic of maritime channel, which leads to a lack of the capability to describe the long-distance multi-scenario maritime communications. Considering the limitations of the existing channel models, we propose a 3D non-stationary GBSM in this paper to address the above-mentioned gaps. The major contributions are summarized as follows:

- a) The proposed channel model can simulate long-distance/time multi-scenario maritime communication channels. The structure of channel will change with the communication distance.
- b) Considering the movement of antennas, the changing environment, and the possibility of deploying massive MIMO antennas on large ships, the birth-death process of clusters in time-array domain and time-variant parameters are used to depict the spatial and temporal

non-stationarities. Furthermore, the large-scale parameters (LSPs) are dealt with by using a spatial filter to realize the spatial consistency of channels.

c) For a more realistic depiction of the sea surface, the classic Pierson-Moskowitz (P-M) spectrum [28] is utilized to study the scattering phenomenon from rough sea surface and simulate the 3D trajectories of antennas. As an environment parameter, the wind speed is introduced to control the height of waves. The propagation through evaporation duct is considered by calculating the maximum and minimum angles of the propagation signal that can be trapped in the duct layer.

d) According to the proposed model, the statistical properties including delay/angular/Doppler power spectrum density (PSD), space-time correlation function (STCF), stationary interval, RMS Doppler spread and RMS delay spread are derived. Moreover, the theoretical results are verified by simulation results and measurement data.

The remainder of this paper is organized as follows. In Section II, the details of the proposed 3D non-stationary GBSM are introduced, including the geometric construction, generation and time evolution of MPCs. Based on the proposed model, the derivation of the statistical properties are presented in Section III. In Section IV, the simulation results and corresponding analyses are given. Finally, conclusions are drawn in Section V.

II. 3D NON-STATIONARY WIDEBAND SHIP-TO-SHIP MIMO GBSM

Considering a typical maritime ship-to-ship communication scenario, the uniform linear arrays (ULAs) are mounted on the ships as Tx and Rx. The simplified model framework is shown in the Fig. 1, and only n_1 -th ($n_1 = 1, \dots, N_1^{pq}(t)$) path, n_2 -th ($n_2 = 1, \dots, N_2^{pq}(t)$) path and LoS path are illustrated to keep it clear. $N_1^{pq}(t)$ and $N_2^{pq}(t)$ are total numbers of the paths generated from sea surface scattering and evaporation duct propagation between p -th ($p = 1, \dots, M_T$) Tx antenna element, i.e., A_p^T , and q -th ($q = 1, \dots, M_R$) Rx antenna element, i.e., A_q^R , at time instant t , respectively. Since the scattering environment is abstracted as clusters, the MPCs can be classified as LoS component, single-bounce components, and multi-bounce components depending on whether the MPC reaches the Rx directly, through one bounce or through multiple bounces. Here, bounces represent reflections, refractions or scatterings caused by the rough sea surface, duct effect, and blockages such as islands and boats. For the multi-bounce propagation, the first-bounce cluster beside the Tx ($C_{n_1}^A$ and $C_{n_2}^A$) and the last-bounce cluster beside the Rx ($C_{n_1}^Z$ and $C_{n_2}^Z$) are shown. In the following, the positions of $C_{n(1/2)}^{A/Z}$ refer to the central locations of clusters. The spheres with grey dots stand for the clusters of evaporation duct scattering paths ($C_{n_2}^A$ and $C_{n_2}^Z$), while the spheres with blue dots represent the clusters of sea surface scattering paths with the centers located at sea level ($C_{n_1}^A$ and $C_{n_1}^Z$). The propagation links between $C_{n(1/2)}^A$ and $C_{n(1/2)}^Z$ are virtual with given delays [29]. When the delays of virtual links are set to zero, the multi-bounce propagation can be reduced to

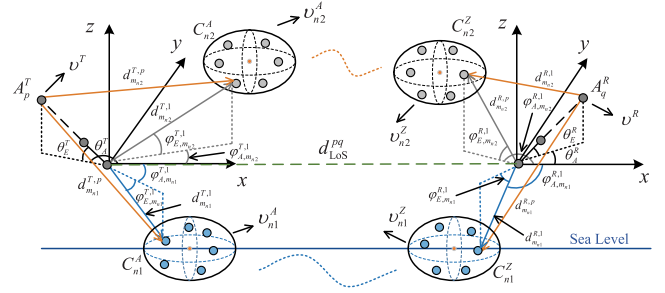


Fig. 1. A 3D non-stationary maritime MIMO GBSM.

single-bounce propagation. Due to the large aperture size of massive MIMO arrays, the cluster sets that can be observed by each antenna element are different. Only on the premise that a pair of clusters can be observed simultaneously by the Tx and Rx, the communication link through this pair of clusters can be formed. For the ship-to-ship communication scenario, Tx, Rx, and clusters should all be moving, which can be described by the velocities v^T , v^R , and $v_{n(1/2)}^{A/Z}$, respectively. The azimuth angle of departure (AAoD) and elevation angle of departure (EAoD) of the m -th ray in n_1 -th or n_2 -th cluster transmitted from A_p^T are denoted by $\varphi_{A,m,n(1/2)}^{T,p}$ and $\varphi_{E,m,n(1/2)}^{T,p}$, and the azimuth angle of arrival (AAoA) and elevation angle of arrival (EAoA) of the m -th ray in n_1 -th or n_2 -th cluster impinging on A_q^R are represented by $\varphi_{A,m,n(1/2)}^{R,q}$ and $\varphi_{E,m,n(1/2)}^{R,q}$, respectively. After the same definition process, the AAoD, EAoD, AAoA and EAoA of the LoS path between A_p^T and A_q^R are determined as $\varphi_{A,LoS}^{T,p}$, $\varphi_{E,LoS}^{T,p}$, $\varphi_{A,LoS}^{R,q}$, and $\varphi_{E,LoS}^{R,q}$. The distance between A_p^T and m -th scatterer in $C_{n_1}^A$ or $C_{n_2}^A$ is denoted by $d_{m,n_1}^{T,1}$ or $d_{m,n_2}^{T,1}$. Similarly, $d_{m,n_1}^{R,1}$ and $d_{m,n_2}^{R,1}$ stand for the distances between A_q^R and m -th scatterer in $C_{n_1}^Z$ and $C_{n_2}^Z$, respectively. Then, the distance between A_p^T/A_q^R and m -th scatterer in $C_{n(1/2)}^A/C_{n(1/2)}^Z$ can be obtained as $d_{m,n(1/2)}^{T,p}$ and $d_{m,n(1/2)}^{R,q}$ according to the geometrical relationships among antenna spacing and transmission distance. Besides, the distance between A_p^T and A_q^R is defined as d_{LoS}^{pq} . The parameters of angles and distances mentioned above are all obtained at the initial moment. The generation method and time-variant property of parameters will be introduced later. The parameters used in the model are summarized in Table I.

The complete channel impulse response (CIR) matrix including the path loss, shadowing, and small-scale fading in maritime channel is given by

$$\mathbf{H} = [PL \cdot SH]^{\frac{1}{2}} \cdot \mathbf{H}_s \quad (1)$$

where PL and SH denote the path loss and shadowing in propagation, respectively. The matrix $\mathbf{H}_s = [h_{pq}(t, \tau)]_{M_T \times M_R}$ consists of small-scale fading CIR of different antenna pairs, and $h_{pq}(t, \tau)$ represents the CIR between the antenna A_p^T and antenna A_q^R . It can be obtained by summing all components in channel, i.e.,

$$h_{pq}(t, \tau) = \sqrt{\frac{K_R}{K_R + 1}} h_{LoS}^{pq}(t, \tau) + \sqrt{\frac{S_1}{K_R + 1}} h_{NL0S_1}^{pq}(t, \tau) + \sqrt{\frac{S_2}{K_R + 1}} h_{NL0S_2}^{pq}(t, \tau) \quad (2)$$

TABLE I
DEFINITION OF CHANNEL SIMULATION PARAMETERS

Parameters	Definitions
A_p^T, A_q^R	The p -th Tx antenna element and q -th Rx antenna element
N_1^{pq}, N_2^{pq}	The numbers of sea surface scattering paths/duct propagation paths between A_p^T and A_q^R
$C_{n_1}^A, C_{n_1}^Z$	The first- and last-bounce clusters for the n_1 -th sea surface scattering path
$C_{n_2}^A, C_{n_2}^Z$	The first- and last-bounce clusters for the n_2 -th evaporation duct propagation path
$v^T, v^R, v_{n(1/2)}^{A/Z}$	The velocities of Tx, Rx and clusters
$\varphi_{A,m_n(1/2)}^{T,1}, \varphi_{E,m_n(1/2)}^{T,1}$	AAoD and EAoD of the m -th ray in $C_{n_1}^A$ or $C_{n_2}^A$ transmitted from A_1^T
$\varphi_{A,m_n(1/2)}^{R,1}, \varphi_{E,m_n(1/2)}^{R,1}$	AAoA and EAoA of the m -th ray in $C_{n_1}^Z$ or $C_{n_2}^Z$ impinging on A_1^R
$\varphi_{A,m_n(1/2)}^{T,p}, \varphi_{E,m_n(1/2)}^{T,p}$	AAoD and EAoD of the m -th ray in $C_{n_1}^A$ or $C_{n_2}^A$ transmitted from A_p^T
$\varphi_{A,m_n(1/2)}^{R,q}, \varphi_{E,m_n(1/2)}^{R,q}$	AAoA and EAoA of the m -th ray in $C_{n_1}^Z$ or $C_{n_2}^Z$ impinging on A_q^R
$\varphi_{A,LoS}^{T,p}, \varphi_{E,LoS}^{T,p}, \varphi_{A,LoS}^{R,q}, \varphi_{E,LoS}^{R,q}$	AAoD, EAoD, AAoA, and EAoA of LoS path between A_p^T and A_q^R
$d_{m_n1}^{T,1}, d_{m_n2}^{T,1}$	The distances between A_1^T and m -th scatterer in $C_{n_1}^A/C_{n_2}^A$
$d_{m_n1}^{R,1}, d_{m_n2}^{R,1}$	The distances between A_1^R and m -th scatterer in $C_{n_1}^Z/C_{n_2}^Z$
$d_{m_n(1/2)}^{T,p}, d_{m_n(1/2)}^{R,q}$	The distances between A_p^T/A_q^R and m -th scatterer in $C_{n_1(1/2)}^A/C_{n_2(1/2)}^Z$
d_{LoS}^{pq}	The length of LoS path between A_p^T and A_q^R
δ_T, δ_R	The spacings of antennas in Tx and Rx arrays
θ_A^T, θ_E^T	Azimuth angle and elevation angle of the Tx antenna array
θ_A^R, θ_E^R	Azimuth angle and elevation angle of the Rx antenna array
$\alpha_{A,n(1/2)}^A, \alpha_{E,n(1/2)}^A$	Azimuth angle and elevation angle of velocities of $C_{n_1}^A/C_{n_2}^A$
$\alpha_{A,n(1/2)}^Z, \alpha_{E,n(1/2)}^Z$	Azimuth angle and elevation angles of velocities of $C_{n_1}^Z/C_{n_2}^Z$
$D_{n_1}^A, D_{n_2}^A$	The distances between Tx and the center of $C_{n_1}^A/C_{n_2}^A$
$D_{n_1}^Z, D_{n_2}^Z$	The distances between Rx and the center of $C_{n_1}^Z/C_{n_2}^Z$

where K_R is the Ricean factor, S_1 and S_2 are power-related coefficients to implement the location-dependent characteristic of the maritime channel. As illustrated in Fig. 2, when the distance between the Tx antenna element and Rx antenna element is in the range of $(0, d_{\text{break}})$, only the LoS path and the sea surface scattering paths can reach Rx (scenario 1). Then, the values of power-related coefficients should be $S_1 = 1$ and $S_2 = 0$. With distance increasing into the range of $[d_{\text{break}}, d_{\text{BLoS}}]$, the scattering paths from evaporation duct are introduced (scenario 2). In this situation, S_1 and S_2 should satisfy the condition $0 < S_1, S_2 < 1$ while $S_1 + S_2 = 1$. When the distance continues to increase and is beyond d_{BLoS} , the LoS path and the sea surface scattering paths will disappear, and only B-LoS communication using the evaporation duct will be retained (scenario 3). At this time, the values of power-related coefficients should be $S_1 = 0$ and $S_2 = 1$, and the value of K_R should be zero.

The distance parameters used to distinguish different scenarios, i.e., d_{break} [17] and d_{BLoS} [8], can be calculated as

$$d_{\text{break}} = \frac{4h_R h_T}{\lambda} \quad (3)$$

$$d_{\text{BLoS}} = \sqrt{h_T^2 + 2R_e h_T} + \sqrt{h_R^2 + 2R_e h_R} \quad (4)$$

where h_T and h_R are the heights of Tx and Rx, respectively, λ is the wavelength of the signal, R_e is the radius of the earth (≈ 6370 km).

The LoS component $h_{\text{LoS}}^{pq}(t, \tau)$ can be written as

$$\begin{aligned} h_{\text{LoS}}^{pq}(t, \tau) &= h_{\text{LoS}}^{pq}(t) \cdot \delta(\tau - \tau_{\text{LoS}}^{pq}(t)) \\ &= \begin{bmatrix} F_{q,V}(\varphi_{E,LoS}^{R,q}, \varphi_{A,LoS}^{R,q}) \\ F_{q,H}(\varphi_{E,LoS}^{R,q}, \varphi_{A,LoS}^{R,q}) \end{bmatrix}^T \begin{bmatrix} e^{j\Theta_{\text{LoS}}^{VV}} & 0 \\ 0 & e^{j\Theta_{\text{LoS}}^{HH}} \end{bmatrix} \\ &\quad \begin{bmatrix} F_{p,V}(\varphi_{E,LoS}^{T,p}, \varphi_{A,LoS}^{T,p}) \\ F_{p,H}(\varphi_{E,LoS}^{T,p}, \varphi_{A,LoS}^{T,p}) \end{bmatrix} e^{j2\pi f_c \tau_{\text{LoS}}^{pq}(t)} \cdot \delta(\tau - \tau_{\text{LoS}}^{pq}(t)) \end{aligned} \quad (5)$$

where f_c is the carrier frequency, $[\cdot]^T$ denotes transposition operation, $F_{q,V/H}$ and $F_{p,V/H}$ are the antenna element field patterns in the vertical polarization and in the horizontal polarization of antenna radiation power pattern [30], which mimic the effect of vertical/horizontal polarization on channel, for A_q^R and A_p^T , respectively, Θ_{LoS}^{VV} and Θ_{LoS}^{HH} are uniformly distributed initial phases within $(0, 2\pi]$, $\tau_{\text{LoS}}^{pq}(t)$ is the time-variant delay of LoS path.

The NLoS components from sea surface and evaporation duct are represented by $h_{\text{NLoS}_1}^{pq}(t, \tau)$ and $h_{\text{NLoS}_2}^{pq}(t, \tau)$, respectively, and they can be expressed as

$$\begin{aligned} h_{\text{NLoS}_1}^{pq}(t, \tau) &= \sum_{n_1=1}^{N_1^{pq}(t)} \sum_{m_{n_1}=1}^{M_{n_1}} h_{m_{n_1}}^{pq}(t) \cdot \delta(\tau - \tau_{m_{n_1}}^{pq}(t)) \\ &= \sum_{n_1=1}^{N_1^{pq}(t)} \sum_{m_{n_1}=1}^{M_{n_1}} \begin{bmatrix} F_{q,V}(\varphi_{E,m_{n_1}}^{R,q}, \varphi_{A,m_{n_1}}^{R,q}) \\ F_{q,H}(\varphi_{E,m_{n_1}}^{R,q}, \varphi_{A,m_{n_1}}^{R,q}) \end{bmatrix}^T \end{aligned}$$

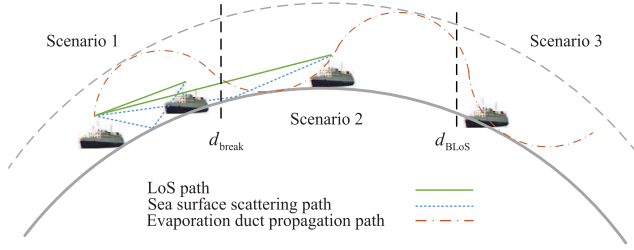


Fig. 2. Illustration of the location-dependent property in ship-to-ship channel.

$$\begin{aligned}
 & \begin{bmatrix} e^{j\Theta_{m_{n1}}^{VV}} & \sqrt{\kappa_{m_{n1}}^{-1}} e^{j\Theta_{m_{n1}}^{VH}} \\ \sqrt{\kappa_{m_{n1}}^{-1}} e^{j\Theta_{m_{n1}}^{HV}} & e^{j\Theta_{m_{n1}}^{HH}} \end{bmatrix} \\
 & \begin{bmatrix} F_{p,V}(\varphi_{E,m_{n1}}^{T,p}, \varphi_{A,m_{n1}}^{T,p}) \\ F_{p,H}(\varphi_{E,m_{n1}}^{T,p}, \varphi_{A,m_{n1}}^{T,p}) \end{bmatrix} \\
 & \sqrt{P_{m_{n1}}^{pq}(t)} \cdot e^{j2\pi f_c \tau_{m_{n1}}^{pq}(t)} \cdot \delta(\tau - \tau_{m_{n1}}^{pq}(t)) \\
 & \quad (6) \\
 h_{\text{NLoS}_2}^{pq}(t, \tau) &= \sum_{n_2=1}^{N_2^{pq}(t)} \sum_{m_{n_2}=1}^{M_{n_2}} h_{m_{n_2}}^{pq}(t) \cdot \delta(\tau - \tau_{m_{n_2}}^{pq}(t)) \\
 &= \sum_{n_2=1}^{N_2^{pq}(t)} \sum_{m_{n_2}=1}^{M_{n_2}} \begin{bmatrix} F_{q,V}(\varphi_{E,m_{n_2}}^{R,q}, \varphi_{A,m_{n_2}}^{R,q}) \\ F_{q,H}(\varphi_{E,m_{n_2}}^{R,q}, \varphi_{A,m_{n_2}}^{R,q}) \end{bmatrix}^T \\
 & \begin{bmatrix} e^{j\Theta_{m_{n_2}}^{VV}} & \sqrt{\kappa_{m_{n_2}}^{-1}} e^{j\Theta_{m_{n_2}}^{VH}} \\ \sqrt{\kappa_{m_{n_2}}^{-1}} e^{j\Theta_{m_{n_2}}^{HV}} & e^{j\Theta_{m_{n_2}}^{HH}} \end{bmatrix} \\
 & \begin{bmatrix} F_{p,V}(\varphi_{E,m_{n_2}}^{T,p}, \varphi_{A,m_{n_2}}^{T,p}) \\ F_{p,H}(\varphi_{E,m_{n_2}}^{T,p}, \varphi_{A,m_{n_2}}^{T,p}) \end{bmatrix} \\
 & \sqrt{P_{m_{n_2}}^{pq}(t)} \cdot e^{j2\pi f_c \tau_{m_{n_2}}^{pq}(t)} \cdot \delta(\tau - \tau_{m_{n_2}}^{pq}(t)) \\
 & \quad (7)
 \end{aligned}$$

where $P_{m_{n(1/2)}}^{pq}(t)$ and $\tau_{m_{n(1/2)}}^{pq}(t)$ are the time-variant power and delay of the m -th ray in the n_1 -th or n_2 -th cluster between the p -th Tx element and q -th Rx element, $\Theta_{m_{n(1/2)}}^{VV}$, $\Theta_{m_{n(1/2)}}^{HH}$, $\Theta_{m_{n(1/2)}}^{VH}$, and $\Theta_{m_{n(1/2)}}^{HV}$ are uniformly distributed initial phases within $(0, 2\pi]$, $\kappa_{m_{n1}}$ and $\kappa_{m_{n2}}$ are the cross polarization power ratios of the two types of NLoS MPCs.

A. 3D Motion of Antennas

The height of a point at sea surface [31] can be expressed as

$$\eta(t) = \sum_{l=1}^L a_l \cos(\omega_l t + \epsilon_l) \quad (8)$$

where L is the number of composite waves, a_l and ω_l are the amplitude and angular frequency of the l -th composite wave, respectively, ϵ_l is the random initial phase which is uniformly distributed in $(0, 2\pi]$.

The amplitude of the composite waves [31] can be calculated as

$$a_l = \sqrt{2S(\omega_l)\Delta\omega} \quad (9)$$

where $S(\omega)$ is the frequency spectrum of sea waves, and $\Delta\omega$ represents the frequency interval between $\omega_l \sim \omega_{l+1}$.

Up to now, a large number of sea spectrums based on observation have been proposed. For the sake of low computational complexity, the classical P-M spectrum [28] was selected, i.e.,

$$S(\omega) = \frac{a_0 g^2}{\omega^5} \exp\left[-\beta \left(\frac{g}{U\omega}\right)^4\right] \quad (10)$$

where $a_0 = 8.1 \times 10^{-3}$ and $\beta = 0.74$ are dimensionless constants, g is the gravitational acceleration and $a_0 g^2 \approx 0.78 \text{ m}^2/\text{s}^4$, U is the wind speed at 19.5 meters above sea level.

By substituting (10) into (9), the sea waves that have similar fluctuation characteristics to the actual sea surface can be simulated. Because the antennas are mounted on ships, they will move in 3D space. The fluctuation of sea waves obtained by using the above method is used to determine the changes in heights of the antennas. Examples of the antenna trajectories at different maritime environments are given in Fig. 3(a) and Fig. 3(b). Here, the antenna arrays are assumed to move linearly with the ships in the $x-y$ plane at constant speeds (10 m/s for Tx and 5 m/s for Rx) and the changes in antenna heights are reflected in the z axis. The simulation time period is 40 s. The antenna initial heights from sea level are 10 m. In Fig. 3(a), the wind speed is 5 m/s at 19.5 m above sea level, while in Fig. 3(b), the wind speed is 10 m/s. From these two figures, it can be observed that the shaking amplitudes of antennas in Fig. 3(b) are larger which is caused by the higher sea waves. Therefore, by using this sea spectrum, we introduce wind speed into our model as a variable to control the trajectories of antennas.

B. Spatial Consistency in Generation of LSPs

The LSPs involved in the channel model include Ricean K-factor, delay spread, angular spread, etc [30], [32], [33]. Due to the motion of Tx and Rx, the antennas will be in different positions at different time, and the LSPs will change accordingly. However, the values of LSPs at adjacent positions should be similar, i.e., spatial consistency. In order to satisfy this condition, the range of motion is divided into many grids. The LSPs will not change at different positions inside one grid, and the LSPs of different grids are correlated. To generate the correlation of LSPs, an exponential spatial filter [34] is used on independent LSPs, which can be expressed as

$$\tilde{l}_{i,j} = \sum_{x=0}^X \sum_{y=0}^Y l_{x,y} h(i-x, j-y) \quad (11)$$

where $l_{x,y}$ and $\tilde{l}_{i,j}$ are independent and correlated values of LSPs at grid (x, y) and (i, j) , respectively, $X \times Y$ is the total number of the grids, and the definition of exponential filter $h(i-x, j-y)$ is

$$h(i-x, j-y) = \exp\left(-\frac{D_l \|i-x, j-y\|}{D_c^S}\right) \quad (12)$$

where D_l is the side length of grids and D_c^S is the correlated distance in time domain.

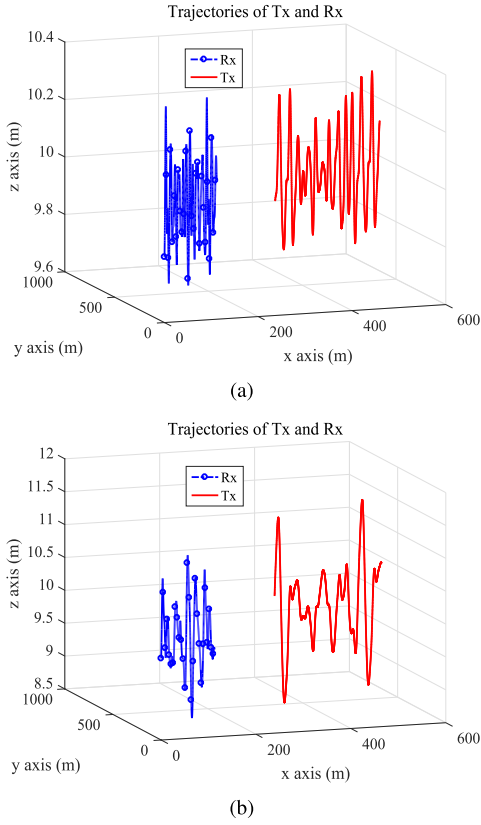


Fig. 3. Simulation of 3D trajectories of ships (antennas) with wind speeds of (a) 5 m/s and (b) 10 m/s.

Based on the positions of antennas at time instant t and corresponding LSPs generated by the above method, the scattering clusters can be generated. Then, the delays and powers of rays in different clusters can be determined.

C. Time-Variant Delay and Power of Rays

1) *Time Evolution of the LoS Component*: For the LoS component, the expression of the vector from p -th Tx antenna element to q -th Rx antenna element is

$$\vec{d}_{\text{LoS}}^{pq}(t) = [\vec{A}_1^R(t) + \vec{\delta}_q^R] - [\vec{A}_1^T(t) + \vec{\delta}_p^T] \quad (13)$$

where $\vec{A}_1^T(t)$ and $\vec{A}_1^R(t)$ are the positions of the first antenna in Tx and Rx array at time instant t , $\vec{\delta}_p^T$ and $\vec{\delta}_q^R$ indicate the vector from A_1^T to A_p^T in Tx array and the vector from A_1^R to A_q^R in Rx array, respectively, and they can be expressed as

$$\vec{\delta}_p^T = \delta_T \cdot (p-1) \cdot [\cos \theta_A^T \cos \theta_E^T \sin \theta_A^T \cos \theta_E^T \sin \theta_E^T] \quad (14)$$

$$\vec{\delta}_q^R = \delta_R \cdot (q-1) \cdot [\cos \theta_A^R \cos \theta_E^R \sin \theta_A^R \cos \theta_E^R \sin \theta_E^R] \quad (15)$$

where δ_T and δ_R are the spacings of the antennas in Tx and Rx arrays, θ_A^T and θ_E^T are the azimuth angle and elevation angle of the Tx antenna array, θ_A^R and θ_E^R are the azimuth angle and elevation angle of the Rx antenna array. The length of LoS path vector is computed as

$$d_{\text{LoS}}^{pq}(t) = \left\| \vec{d}_{\text{LoS}}^{pq}(t) \right\|. \quad (16)$$

Meanwhile, the AAoD, EAoD, AAoA, and EAoA of LoS path can be obtained by the vector $\vec{d}_{\text{LoS}}^{pq}(t)$ and can be expressed as

$$\varphi_{A,\text{LoS}}^{T,p}(t) = \arctan_2(Y_{\vec{d}_{\text{LoS}}^{pq}(t)}, X_{\vec{d}_{\text{LoS}}^{pq}(t)}) \quad (17)$$

$$\varphi_{E,\text{LoS}}^{T,p}(t) = \arcsin(Z_{\vec{d}_{\text{LoS}}^{pq}(t)}, d_{\text{LoS}}^{pq}(t)) \quad (18)$$

$$\varphi_{A,\text{LoS}}^{R,q}(t) = \pi + \varphi_{A,\text{LoS}}^{T,p}(t) \quad (19)$$

$$\varphi_{E,\text{LoS}}^{R,q}(t) = -\varphi_{E,\text{LoS}}^{T,p}(t) \quad (20)$$

where $X_{(\cdot)}$, $Y_{(\cdot)}$, and $Z_{(\cdot)}$ represent the x , y and z components of corresponding vector, $\arctan_2(\cdot)$ and $\arcsin(\cdot)$ denote the four-quadrant inverse tangent function and inverse sine function, respectively.

2) *Birth of Clusters Beside the Tx*: Depending on the EAoDs, the propagation of scattering paths through the sea surface or the evaporation duct can be distinguished. Thus, according to the ranges of the angles, two kinds of clusters will be generated separately.

For the propagation through evaporation duct, the maximum and minimum values of the elevation angles of the paths which can be trapped by evaporation duct layer [35] are

$$\theta_{\text{max,min}}^T = \pm \sqrt{2 \left(\frac{1}{n(0)} \frac{dn(z)}{dz} \Big|_{z=h_\delta} + \frac{1}{R_e} \right) (h_T - h_\delta)} \quad (21)$$

where h_δ is the duct height, $n(z)$ is the refractive index, z represents the height, $n(0) \approx 1.00035$ is the refractive index at surface. Therefore, $\frac{dn(z)}{dz}$ is the vertical gradient of the refractive index which can be calculated as

$$\frac{dn(z)}{dz} = \left(\frac{dM(z)}{dz} - 0.157 \right) \times 10^{-6} \quad (22)$$

where $M(z)$ is the modified refractivity, and the refractivity profile in evaporation duct [36] can be expressed as

$$M(z) = M_0 + 0.125z - 0.125h_\delta \ln \left(\frac{z+z_0}{z_0} \right) \quad (23)$$

where $M_0 = 315$ M-units is the value of modified refractivity at sea surface, and $z_0 = 1.5 \times 10^{-4}$ m is the aerodynamic roughness length. The refractivity profile is obtained under the assumption of neutral troposphere conditions and the standard temperature (15°C). According to the trapping beamwidth, the ranges of elevation angles of scattering paths at Tx side are divided as shown in Fig. 4.

Due to the limited range of angles, the angles of departure (AoDs) of clusters beside the Tx are assumed to follow truncated Gaussian distribution [37], i.e.,

$$f_\theta(\theta) = \frac{\frac{1}{\sigma_\theta \sqrt{2\pi}} \exp \left(\frac{-(\theta - \mu_\theta)^2}{2\sigma_\theta^2} \right)}{\Phi \left(\frac{b - \mu_\theta}{\sigma_\theta} \right) - \Phi \left(\frac{a - \mu_\theta}{\sigma_\theta} \right)} I_{(a,b)}(\theta) \quad (24)$$

$$I_{(a,b)}(\theta) = \begin{cases} 1 & a \leq \theta \leq b \\ 0 & \text{otherwise} \end{cases} \quad (25)$$

where θ represents EAoDs or AAoDs, μ_θ and σ_θ represent the corresponding mean value and angular spread, and Φ is the standard normal cumulative distribution function (CDF). For EAoD of the cluster from sea surface ($C_{n_1}^A$), i.e., ϕ_{E,n_1}^T , the values of a and b are $-\pi/2$ and θ_{min} , respectively. For EAoD

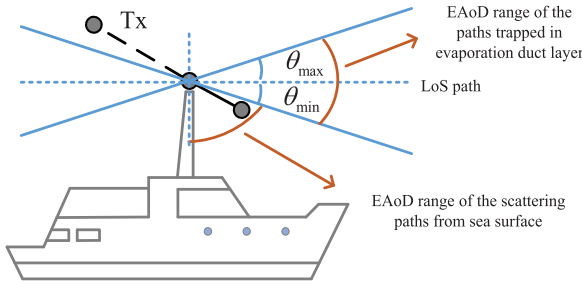


Fig. 4. Illustration of EAOd ranges of different scattering paths.

of the cluster from evaporation duct ($C_{n_2}^A$), i.e., ϕ_{E,n_2}^T , the values of a and b are θ_{\min} and θ_{\max} , respectively. Besides, the AAoD of $C_{n_1}^A$ (ϕ_{A,n_1}^T) follows normal distribution (i.e., $a = -\infty$ and $b = \infty$), while the AAoD of $C_{n_2}^A$ (ϕ_{A,n_2}^T) is assumed to follow truncated Gaussian distribution with $a = \varphi_{A,LoS}^{T,p}(t_{n_2}^0) + \theta_{\min}$ and $b = \varphi_{A,LoS}^{T,p}(t_{n_2}^0) + \theta_{\max}$, where $t_{n_2}^0$ denotes the initial generation moment of $C_{n_2}^A$.

Then, the center positions of scattering clusters $C_{n_1}^A$ and $C_{n_2}^A$ at initial generation moments ($t_{n_1}^0/t_{n_2}^0$) can be determined respectively as

$$\vec{C}_{n_1}^A(t_{n_1}^0) = \vec{A}_1^T(t_{n_1}^0) + D_{n_1}^A \cdot \vec{r}_{n_1}^A \quad (26)$$

$$\vec{C}_{n_2}^A(t_{n_2}^0) = \vec{A}_1^T(t_{n_2}^0) + D_{n_2}^A \cdot \vec{r}_{n_2}^A \quad (27)$$

where $\vec{r}_{n_1}^A$ and $\vec{r}_{n_2}^A$ are direction vectors from Tx to $C_{n_1}^A/C_{n_2}^A$ which can be expressed as

$$\vec{r}_{n_1}^A = [\cos\phi_{A,n_1}^T \cos\phi_{E,n_1}^T \sin\phi_{A,n_1}^T \cos\phi_{E,n_1}^T \sin\phi_{E,n_1}^T] \quad (28)$$

$$\vec{r}_{n_2}^A = [\cos\phi_{A,n_2}^T \cos\phi_{E,n_2}^T \sin\phi_{A,n_2}^T \cos\phi_{E,n_2}^T \sin\phi_{E,n_2}^T]. \quad (29)$$

The distance between Tx and the center of $C_{n_2}^A$ ($D_{n_2}^A$) can be produced by the exponential distribution [29], [34]. Because the center of $C_{n_1}^A$ should be at sea level, the distance between Tx and the center of $C_{n_1}^A$ ($D_{n_1}^A$) can be calculated as

$$D_{n_1}^A = Z_{\vec{A}_1^T(t_{n_1}^0)} / \cos\left(-\frac{\pi}{2} - \phi_{E,n_1}^T\right) \quad (30)$$

where $Z_{\vec{A}_1^T(t_{n_1}^0)}$ is the z component of the vector $\vec{A}_1^T(t_{n_1}^0)$.

3) *Birth of Clusters Beside the Rx*: According to the symmetry of the channel, the angles of the clusters beside the Rx can be generated by using the same method. The AAoA of cluster from sea surface ($C_{n_1}^Z$), i.e., ϕ_{A,n_1}^R , is assumed to follow normal distribution, and the EAOA of $C_{n_1}^Z$, i.e., ϕ_{E,n_1}^R , is assumed to follow truncated Gaussian distribution with $a = -\pi/2$ and $b = \theta_{\min}$. For the clusters from evaporation duct ($C_{n_2}^Z$), the EAOA, i.e., ϕ_{E,n_2}^R , follows truncated Gaussian distribution with the same limited range as that beside the Tx, while the AAoA, i.e., ϕ_{A,n_2}^R , follows truncated Gaussian distribution with the range $[\varphi_{A,LoS}^{R,q}(t_{n_2}^0) + \theta_{\min} \varphi_{A,LoS}^{R,q}(t_{n_2}^0) + \theta_{\max}]$. After the same generation process of distances from Rx to clusters, the center positions of scattering clusters $C_{n_1}^Z$ and $C_{n_2}^Z$ at initial generation moment can be obtained as

$$\vec{C}_{n_1}^Z(t_{n_1}^0) = \vec{A}_1^R(t_{n_1}^0) + D_{n_1}^Z \cdot \vec{r}_{n_1}^Z \quad (31)$$

$$\vec{C}_{n_2}^Z(t_{n_2}^0) = \vec{A}_1^R(t_{n_2}^0) + D_{n_2}^Z \cdot \vec{r}_{n_2}^Z \quad (32)$$

where $D_{n_1}^Z$ and $D_{n_2}^Z$ represent the distances between Rx and the center of $C_{n_1}^Z/C_{n_2}^Z$, respectively, $\vec{r}_{n_1}^Z$ and $\vec{r}_{n_2}^Z$ are direction

vectors from Rx to $C_{n_1}^Z/C_{n_2}^Z$ which can be expressed as

$$\vec{r}_{n_1}^Z = [\cos\phi_{A,n_1}^R \cos\phi_{E,n_1}^R \sin\phi_{A,n_1}^R \cos\phi_{E,n_1}^R \sin\phi_{E,n_1}^R] \quad (33)$$

$$\vec{r}_{n_2}^Z = [\cos\phi_{A,n_2}^R \cos\phi_{E,n_2}^R \sin\phi_{A,n_2}^R \cos\phi_{E,n_2}^R \sin\phi_{E,n_2}^R]. \quad (34)$$

4) *Spatial Dispersions of Scatterers in Clusters*: Considering the dispersions of scatterers within clusters, the positions of m -th ray in the clusters $C_{n(1/2)}^A$ and $C_{n(1/2)}^Z$ can be calculated as

$$\vec{C}_{m,n(1/2)}^A(t_{n(1/2)}^0) = \vec{C}_{n(1/2)}^A(t_{n(1/2)}^0) + \Delta \vec{d}_{m,n(1/2)}^A \quad (35)$$

$$\vec{C}_{m,n(1/2)}^Z(t_{n(1/2)}^0) = \vec{C}_{n(1/2)}^Z(t_{n(1/2)}^0) + \Delta \vec{d}_{m,n(1/2)}^Z \quad (36)$$

$$\Delta \vec{d}_{m,n(1/2)}^{A/Z} = \begin{bmatrix} \Delta x_{m,n(1/2)}^{A/Z} & \Delta y_{m,n(1/2)}^{A/Z} & \Delta z_{m,n(1/2)}^{A/Z} \end{bmatrix} \quad (37)$$

where $\Delta x_{m,n(1/2)}^{A/Z}$, $\Delta y_{m,n(1/2)}^{A/Z}$, and $\Delta z_{m,n(1/2)}^{A/Z}$ are all subject to normal distributions with given standard deviations $\sigma_{n(1/2)}^{x/y/z}$ and zero means.

Specially, $\Delta z_{m,n(1/2)}^{A/Z}$ in clusters generating from rough sea surface will depend on the sea surface height. Since wave height also follows normal distribution approximately [38], the standard deviation $\sigma_{n_1}^z$ of $\Delta z_{m,n(1/2)}^{A/Z}$ can be approximated as the standard deviation of wave height. By deriving the relationship between $\sigma_{n_1}^z$ and sea surface height, the influence of different wave levels on the dispersion of scatterers can be reflected.

As mentioned above, we use $\eta(t)$ in (8) to describe the wave fluctuations. The expectation of $\eta(t)$ is 0. Therefore, the variance of $\eta(t)$ is equal to the mean-square value of $\eta(t)$. In fact, the sea surface height autocorrelation is the inverse Fourier transform of the sea spectrum $S(\omega)$ [39], i.e.,

$$R_{\eta\eta}(\Delta t_\eta) = \mathbb{E}[\eta(t)\eta(t + \Delta t_\eta)] = \int_0^\infty S(\omega) e^{j\omega\Delta t_\eta} d\omega \quad (38)$$

where $\mathbb{E}[\cdot]$ represents the operation of computing expectation, and Δt_η is the time difference.

Then, by setting $\Delta t_\eta = 0$ in (38), the variance of wave height can be calculated as

$$D[\eta] = \mathbb{E}[\eta^2(t)] = R_{\eta\eta}(0) = \int_0^\infty S(\omega) d\omega. \quad (39)$$

Combine (39) and P-M spectrum described in (10), the standard deviation $\sigma_{n_1}^z$ can be obtained from the zero-order moment of the spectrum [40], i.e.,

$$\sigma_{n_1}^z = \sqrt{\mathbb{E}[\eta^2(t)]} = \sqrt{\frac{a_0 U^4}{4\beta g^2}}. \quad (40)$$

5) *Time Evolution of the NLoS Components*: Considering the mobility of Tx/Rx and cluster, the distance vectors $\vec{d}_{m,n(1/2)}^{T,p}(t)$ from Tx to $C_{m,n(1/2)}^A$ and $\vec{d}_{m,n(1/2)}^{R,q}(t)$ from Rx to $C_{m,n(1/2)}^Z$ are time-variant, which can be calculated as

$$\begin{aligned} \vec{d}_{m,n(1/2)}^{T,p}(t) &= \vec{C}_{m,n(1/2)}^A(t_{n(1/2)}^0) \\ &+ \int_{t_{n(1/2)}^0}^t \vec{v}_{n(1/2)}^A(t) dt - [\vec{A}_1^T(t) + \vec{\delta}_p^T] \end{aligned} \quad (41)$$

$$\begin{aligned} \vec{d}_{m_n(1/2)}^{R,q}(t) &= \vec{A}_1^R(t) + \vec{\delta}_q^R \\ &\quad - [\vec{C}_{m_n(1/2)}^Z(t_{n(1/2)}^0) + \int_{t_{n(1/2)}^0}^t \vec{v}_{n(1/2)}^Z(t) dt] \end{aligned} \quad (42)$$

where $\vec{v}_{n(1/2)}^A(t)$ and $\vec{v}_{n(1/2)}^Z(t)$ are the time-variant velocity vectors of clusters and can be expressed as

$$\vec{v}_{n(1/2)}^A(t) = v_{n(1/2)}^A(t) \cdot \begin{bmatrix} \cos \alpha_{A,n(1/2)}^A & \cos \alpha_{E,n(1/2)}^A \\ \sin \alpha_{A,n(1/2)}^A & \cos \alpha_{E,n(1/2)}^A \\ \sin \alpha_{E,n(1/2)}^A & \end{bmatrix}^T \quad (43)$$

$$\vec{v}_{n(1/2)}^Z(t) = v_{n(1/2)}^Z(t) \cdot \begin{bmatrix} \cos \alpha_{A,n(1/2)}^Z & \cos \alpha_{E,n(1/2)}^Z \\ \sin \alpha_{A,n(1/2)}^Z & \cos \alpha_{E,n(1/2)}^Z \\ \sin \alpha_{E,n(1/2)}^Z & \end{bmatrix}^T \quad (44)$$

where $\alpha_{A,n(1/2)}^A$ and $\alpha_{E,n(1/2)}^A$ stand for the azimuth and elevation angle of velocities of $C_{n_1}^A/C_{n_2}^A$, while the azimuth and elevation angle of velocities of $C_{n_1}^Z/C_{n_2}^Z$ are represented by $\alpha_{A,n(1/2)}^Z$ and $\alpha_{E,n(1/2)}^Z$, respectively.

The distance from p -th Tx antenna element to $C_{n_1}^A/C_{n_2}^A$ and the distance from q -th Rx antenna element to $C_{n_1}^Z/C_{n_2}^Z$ are determined by $d_{m_n(1/2)}^{T,p}(t) = \|\vec{d}_{m_n(1/2)}^{T,p}(t)\|$ and $d_{m_n(1/2)}^{R,q}(t) = \|\vec{d}_{m_n(1/2)}^{R,q}(t)\|$, respectively. The sum of these two time-variant distances can be expressed as $D_{m_n(1/2)}^{pq}(t) = d_{m_n(1/2)}^{T,p}(t) + d_{m_n(1/2)}^{R,q}(t)$.

Similar to the LoS path, the AoDs and the angles of arrival (AoAs) of m -th ray in n_1 -th or n_2 -th cluster can be calculated based on the vectors $\vec{d}_{m_n(1/2)}^{T,p}$ and $\vec{d}_{m_n(1/2)}^{R,q}$, which can be expressed as

$$\varphi_{A,m_n(1/2)}^{T,p}(t) = \arctan_2(Y_{\vec{d}_{m_n(1/2)}^{T,p}}(t), X_{\vec{d}_{m_n(1/2)}^{T,p}}(t)) \quad (45)$$

$$\varphi_{E,m_n(1/2)}^{T,p}(t) = \arcsin(Z_{\vec{d}_{m_n(1/2)}^{T,p}}(t), d_{m_n(1/2)}^{T,p}(t)) \quad (46)$$

$$\varphi_{A,m_n(1/2)}^{R,q}(t) = \arctan_2(Y_{\vec{d}_{m_n(1/2)}^{R,q}}(t), X_{\vec{d}_{m_n(1/2)}^{R,q}}(t)) \quad (47)$$

$$\varphi_{E,m_n(1/2)}^{R,q}(t) = \arcsin(Z_{\vec{d}_{m_n(1/2)}^{R,q}}(t), d_{m_n(1/2)}^{R,q}(t)). \quad (48)$$

Due to the time-variant transmission distance, the delay of m -th ray in n_1 -th or n_2 -th cluster will change over time, and can be modeled as

$$\tau_{m_n(1/2)}^{pq}(t) = \frac{D_{m_n(1/2)}^{pq}(t)}{c} + \tilde{\tau}_{m_n(1/2)} \quad (49)$$

where c is the speed of light, $\tilde{\tau}_{m_n(1/2)}$ is the delay of virtual link between $C_{m_n(1/2)}^A$ and $C_{m_n(1/2)}^Z$ and is determined as $\tilde{\tau}_{m_n(1/2)} = \tilde{D}_{m_n(1/2)}/c + \tau_{n(1/2)}^{\text{link}}$, where $\tilde{D}_{m_n(1/2)}$ is the distance between $C_{m_n(1/2)}^A$ and $C_{m_n(1/2)}^Z$, $\tau_{n(1/2)}^{\text{link}}$ is a non-negative variable which is assumed to follow exponential distribution [41] and can be generated as

$$\tau_{n(1/2)}^{\text{link}} = -r_\tau^{1/2} \sigma_\tau^{1/2} \cdot \ln u_{n(1/2)} \quad (50)$$

where $r_\tau^{1/2}$ and $\sigma_\tau^{1/2}$ are the delay scalar and delay spread of two kinds of NLoS components [42], respectively, $u_{n(1/2)}$ is uniformly distributed within (0,1). Besides, the delay of LoS component is $\tau_{\text{LoS}}^{pq}(t) = d_{\text{LoS}}^{pq}(t)/c$.

Then, the time-variant ray power can be calculated according to a single slope exponential PDP [30] and can be represented as

$$P_{m_n(1/2)}^{pq}(t) = \left[\exp \left(-\tau_{m_n(1/2)}^{pq}(t) \frac{r_\tau^{1/2} - 1}{r_\tau^{1/2} \sigma_\tau^{1/2}} \right) 10 \frac{Z_{n(1/2)}}{10} \right] \quad (51)$$

where $Z_{n(1/2)}$ is the per cluster shadowing in dB. These parameter values of different clusters are distinguished according to their subscripts.

At last, by performing a normalization operation, the powers are obtained as

$$P_{m_{n_1}}^{pq}(t) = P_{m_{n_1}}^{pq}(t) / \sum_{n_1=1}^{N_1^{pq}(t)} \sum_{m_{n_1}=1}^{M_{n_1}} P_{m_{n_1}}^{pq}(t) \quad (52)$$

$$P_{m_{n_2}}^{pq}(t) = P_{m_{n_2}}^{pq}(t) / \sum_{n_2=1}^{N_2^{pq}(t)} \sum_{m_{n_2}=1}^{M_{n_2}} P_{m_{n_2}}^{pq}(t). \quad (53)$$

6) Birth-Death Process of Clusters Along Time-Array Axes:

For the ship-to-ship communication scenario, the movement of Tx/Rx and the variation of maritime environment lead to the birth-death process of clusters in the time domain. Similarly, whether the clusters can be observed by antennas in the array can be regarded as the birth-death process of clusters along the array axis. To describe the disappearance and survival of clusters, the Poisson processes was adopted [43], [44]. The probability P_s^T , P_s^R of a cluster surviving over time period Δt_s and antenna element spacing $\Delta \xi_T$ at the Tx side, and over Δt_s and antenna element spacing $\Delta \xi_R$ at the Rx side are given as below, respectively,

$$P_s^T(\Delta t_s, \Delta \xi_T) = \exp \left[-\lambda_R \left(\frac{\int_{t_0}^{t_0+\Delta t_s} v^T(t) dt}{D_c^S} + \frac{\Delta \xi_T}{D_c^A} \right) \right] \quad (54)$$

$$P_s^R(\Delta t_s, \Delta \xi_R) = \exp \left[-\lambda_R \left(\frac{\int_{t_0}^{t_0+\Delta t_s} v^R(t) dt}{D_c^S} + \frac{\Delta \xi_R}{D_c^A} \right) \right] \quad (55)$$

where λ_R is the recombination rate accounting for the disappearance of clusters, D_c^A is the correlated distance in array domain, and t_0 is the initial simulation time.

Since the paths only exist when the paired clusters of Tx and Rx sides remain simultaneously, the joint survival probability can be calculated as

$$P_{\text{survival}}(\Delta t_s, \Delta \xi_T, \Delta \xi_R) = P_s^T(\Delta t_s, \Delta \xi_T) \cdot P_s^R(\Delta t_s, \Delta \xi_R). \quad (56)$$

At the same time, there are some new clusters generated over time period Δt_s . According to Poisson process, the expectation of the number of newly generated clusters [41] is determined as

$$\mathbb{E}(N_{\text{new}}) = \frac{\lambda_G}{\lambda_R} (1 - P_{\text{survival}}(\Delta t_s, \Delta \xi_T, \Delta \xi_R)) \quad (57)$$

where λ_G is the generation rate of clusters.

III. STATISTICAL PROPERTIES OF CHANNEL MODEL

A. Time-Variant Transfer Function

The time-variant transfer function between the antenna A_p^T and antenna A_q^R can be obtained by the Fourier transform of time-variant CIR $h_{pq}(t, \tau)$ with respect to delay τ , i.e.,

$$\begin{aligned} H_{pq}(t, f) &= \int_{-\infty}^{\infty} h_{pq}(t, \tau) e^{-j2\pi f \tau} d\tau \\ &= h_{\text{LoS}}^{pq}(t) e^{-j2\pi f \tau_{\text{LoS}}^{pq}(t)} + \sum_{n_1=1}^{N_1^{pq}(t)} \sum_{m_{n_1}=1}^{M_{n_1}} h_{m_{n_1}}^{pq}(t) e^{-j2\pi f \tau_{m_{n_1}}^{pq}(t)} \\ &\quad + \sum_{n_2=1}^{N_2^{pq}(t)} \sum_{m_{n_2}=1}^{M_{n_2}} h_{m_{n_2}}^{pq}(t) e^{-j2\pi f \tau_{m_{n_2}}^{pq}(t)}. \end{aligned} \quad (58)$$

B. Delay PSD

The time-variant delay PSD $\Lambda_{pq}(t, \tau)$ reflects the time-dependent characteristic of the delays and powers for rays between the antenna A_p^T and the antenna A_q^R , and can be calculated as

$$\begin{aligned} \Lambda_{pq}(t, \tau) &= \sum_{n_1=1}^{N_1^{pq}(t)} \sum_{m_{n_1}=1}^{M_{n_1}} \tilde{P}_{m_{n_1}}^{pq}(t) \delta(\tau - \tau_{m_{n_1}}^{pq}(t)) \\ &\quad + \sum_{n_2=1}^{N_2^{pq}(t)} \sum_{m_{n_2}=1}^{M_{n_2}} \tilde{P}_{m_{n_2}}^{pq}(t) \delta(\tau - \tau_{m_{n_2}}^{pq}(t)) \end{aligned} \quad (59)$$

where $\tilde{P}_{m_{n_1}}^{pq}(t) = S_1 \cdot P_{m_{n_1}}^{pq}(t)$ and $\tilde{P}_{m_{n_2}}^{pq}(t) = S_2 \cdot P_{m_{n_2}}^{pq}(t)$ are the power controlled by the power-related coefficients. Changes of the channel environment will affect the evolution of the clusters, and will further affect the delay PSD.

C. Stationary Interval

In order to evaluate the time-variation of channel, the stationary interval can be calculated. It is the maximum time duration in which the channel can be regarded as wide sense stationary (WSS). As a method for measuring stationary interval, the local region of stationarity (LRS) method [45] calculates the maximum time length within which the correlation coefficient of two delay PSDs exceeds a given threshold, which is usually set at 80% [45], i.e.,

$$I(t) = \max \{ \Delta t | c_{\Lambda}(t, \Delta t) \geq c_{\text{thresh}} \} \quad (60)$$

where c_{thresh} is the value of threshold, and c_{Λ} is the correlation coefficient that can be calculated as

$$c_{\Lambda}(t, \Delta t) = \frac{\int \Lambda(t, \tau) \Lambda(t + \Delta t, \tau) d\tau}{\max \{ \int \Lambda^2(t, \tau) d\tau, \int \Lambda^2(t + \Delta t, \tau) d\tau \}}. \quad (61)$$

D. Angular PSD

The relationship between the power and angles can be presented in angular PSD [46], and the angular PSD for AAoDs and EAoDs of rays between the antenna A_p^T and

antenna A_q^R can be expressed as

$$\begin{aligned} \Lambda_{pq}^{T,A}(t, \varphi_A^T) &= \sum_{n_1=1}^{N_1^{pq}(t)} \sum_{m_{n_1}=1}^{M_{n_1}} \tilde{P}_{m_{n_1}}^{pq}(t) \delta(\varphi_A^T - \varphi_{A, m_{n_1}}^{T,p}(t)) \\ &\quad + \sum_{n_2=1}^{N_2^{pq}(t)} \sum_{m_{n_2}=1}^{M_{n_2}} \tilde{P}_{m_{n_2}}^{pq}(t) \delta(\varphi_A^T - \varphi_{A, m_{n_2}}^{T,p}(t)) \end{aligned} \quad (62)$$

$$\begin{aligned} \Lambda_{pq}^{T,E}(t, \varphi_E^T) &= \sum_{n_1=1}^{N_1^{pq}(t)} \sum_{m_{n_1}=1}^{M_{n_1}} \tilde{P}_{m_{n_1}}^{pq}(t) \delta(\varphi_E^T - \varphi_{E, m_{n_1}}^{T,p}(t)) \\ &\quad + \sum_{n_2=1}^{N_2^{pq}(t)} \sum_{m_{n_2}=1}^{M_{n_2}} \tilde{P}_{m_{n_2}}^{pq}(t) \delta(\varphi_E^T - \varphi_{E, m_{n_2}}^{T,p}(t)). \end{aligned} \quad (63)$$

E. Local STCF

To describe the correlation characteristics between $h_{pq}(t)$ and $h_{p'q'}(t - \Delta t)$, the local STCF is defined as

$$R_{pq, p'q'}(t, f; \Delta \xi, \Delta t) = \mathbb{E} \{ h_{pq}(t) h_{p'q'}^*(t - \Delta t) \}. \quad (64)$$

According to (2), the local STCF can be written as the summation of LoS component correlation and two kinds of NLoS components correlation, i.e.,

$$\begin{aligned} R_{pq, p'q'}(t, f; \Delta \xi, \Delta t) &= \frac{K_R}{K_R + 1} R_{pq, p'q'}^{\text{LoS}}(t, f; \Delta \xi, \Delta t) \\ &\quad + \frac{1}{K_R + 1} \left[\sum_{n_1=1}^{N_1^{pq}(t)} R_{pq, p'q', n_1}^{\text{NLoS}_1}(t, f; \Delta \xi, \Delta t) \right. \\ &\quad \left. + \sum_{n_2=1}^{N_2^{pq}(t)} R_{pq, p'q', n_2}^{\text{NLoS}_2}(t, f; \Delta \xi, \Delta t) \right]. \end{aligned} \quad (65)$$

The correlation of the LoS component and NLoS components are calculated as

$$\begin{aligned} R_{pq, p'q'}^{\text{LoS}}(t, f; \Delta \xi, \Delta t) &= e^{j \frac{2\pi}{\lambda} [d_{\text{LoS}}^{pq}(t) - d_{\text{LoS}}^{p'q'}(t - \Delta t)]} \end{aligned} \quad (66)$$

$$\begin{aligned} R_{pq, p'q', n_1}^{\text{NLoS}_1}(t, f; \Delta \xi, \Delta t) &= P_{\text{survival}}(\Delta t, \Delta \xi) \\ &\quad \cdot \mathbb{E} \left\{ \sum_{m_{n_1}=1}^{M_{n_1}} a_{m_{n_1}} e^{j \frac{2\pi}{\lambda} [D_{m_{n_1}}^{pq}(t) - D_{m_{n_1}}^{p'q'}(t - \Delta t)]} \right\} \end{aligned} \quad (67)$$

$$\begin{aligned} R_{pq, p'q', n_2}^{\text{NLoS}_2}(t, f; \Delta \xi, \Delta t) &= P_{\text{survival}}(\Delta t, \Delta \xi) \\ &\quad \cdot \mathbb{E} \left\{ \sum_{m_{n_2}=1}^{M_{n_2}} a_{m_{n_2}} e^{j \frac{2\pi}{\lambda} [D_{m_{n_2}}^{pq}(t) - D_{m_{n_2}}^{p'q'}(t - \Delta t)]} \right\} \end{aligned} \quad (68)$$

where $\Delta \xi = \{ \Delta \xi_T, \Delta \xi_R \}$, $\Delta \xi_T = \left\| \vec{\delta}_{p'}^T - \vec{\delta}_p^T \right\|$, $\Delta \xi_R = \left\| \vec{\delta}_{q'}^R - \vec{\delta}_q^R \right\|$, $a_{m_{n_1}} = \sqrt{\tilde{P}_{m_{n_1}}^{pq}(t) \tilde{P}_{m_{n_1}}^{p'q'}(t - \Delta t)}$, $a_{m_{n_2}} = \sqrt{\tilde{P}_{m_{n_2}}^{pq}(t) \tilde{P}_{m_{n_2}}^{p'q'}(t - \Delta t)}$, and $P_{\text{survival}}(\Delta t, \Delta \xi)$ is the joint

probability that a cluster can survive from $t - \Delta t$ to t and over antenna element spacing $\Delta\xi$.

By assigning $\Delta\xi$ to 0 in STCF, the temporal ACF can be computed. Moreover, the spatial CCF can be obtained by setting $\Delta t = 0$.

F. Doppler PSD

The Doppler PSD can be obtained as the Fourier transform of temporal ACF [42] and can be expressed as,

$$S_{pq,p'q'}(t, f; \nu) = \int_{-\infty}^{\infty} R_{pq,p'q'}(t, f; 0, \Delta t) e^{-j2\pi\nu\Delta t} d\Delta t \quad (69)$$

where ν represents the Doppler frequency.

G. RMS Doppler Spread and RMS Delay Spread

The instantaneous Doppler frequency describes phase change rate caused by time-variant path length. The frequency shifts of m -th ray in n_1 -th path or n_2 -th path between A_p^T and A_q^R [47] can be computed as

$$\nu_{m_{n_1}}^{pq}(t) = \frac{1}{\lambda} \frac{d[D_{m_{n_1}}^{pq}(t)]}{dt} \quad (70)$$

$$\nu_{m_{n_2}}^{pq}(t) = \frac{1}{\lambda} \frac{d[D_{m_{n_2}}^{pq}(t)]}{dt}. \quad (71)$$

By calculating the second-order moment of the Doppler frequency, the RMS Doppler spread, which is used to quantify the dispersion of signals in Doppler frequency domain, can be obtained as

$$\sigma_{\nu}^{pq}(t) = \sqrt{\overline{\nu_{pq}^2(t)} - \bar{\nu}_{pq}^2(t)} \quad (72)$$

where

$$\begin{aligned} \overline{\nu_{pq}^2(t)} &= \sum_{n_1=1}^{N_1^{pq}(t)} \sum_{m_{n_1}=1}^{M_{n_1}} \tilde{P}_{m_{n_1}}^{pq}(t) \nu_{m_{n_1}}^{pq}(t)^2 \\ &+ \sum_{n_2=1}^{N_2^{pq}(t)} \sum_{m_{n_2}=1}^{M_{n_2}} \tilde{P}_{m_{n_2}}^{pq}(t) \nu_{m_{n_2}}^{pq}(t)^2 \end{aligned} \quad (73)$$

$$\begin{aligned} \bar{\nu}_{pq}(t) &= \sum_{n_1=1}^{N_1^{pq}(t)} \sum_{m_{n_1}=1}^{M_{n_1}} \tilde{P}_{m_{n_1}}^{pq}(t) \nu_{m_{n_1}}^{pq}(t) \\ &+ \sum_{n_2=1}^{N_2^{pq}(t)} \sum_{m_{n_2}=1}^{M_{n_2}} \tilde{P}_{m_{n_2}}^{pq}(t) \nu_{m_{n_2}}^{pq}(t). \end{aligned} \quad (74)$$

To specify the dispersion of signal in delay domain, the RMS delay spread is calculated by using the same calculation method as the RMS Doppler spread, which can be expressed as

$$\sigma_{\tau}^{pq}(t) = \sqrt{\overline{\tau_{pq}^2(t)} - \bar{\tau}_{pq}^2(t)} \quad (75)$$

where

$$\begin{aligned} \overline{\tau_{pq}^2(t)} &= \sum_{n_1=1}^{N_1^{pq}(t)} \sum_{m_{n_1}=1}^{M_{n_1}} \tilde{P}_{m_{n_1}}^{pq}(t) \tau_{m_{n_1}}^{pq}(t)^2 \\ &+ \sum_{n_2=1}^{N_2^{pq}(t)} \sum_{m_{n_2}=1}^{M_{n_2}} \tilde{P}_{m_{n_2}}^{pq}(t) \tau_{m_{n_2}}^{pq}(t)^2 \end{aligned} \quad (76)$$

TABLE II
PARAMETERS FOR CHANNEL SIMULATION

Parameters	Mean	Standard deviation
K_R	18.1 (dB) [48]	1.3 (dB)
$\sigma_{\tau}^1 / \sigma_{\tau}^2$	-6.6/-6.5 (dB)	1.2/1 (dB)
$\sigma_{\phi_{E,n_1}^{T/R}} / \sigma_{\phi_{A,n_1}^{T/R}}$	30.9/65.9 ($^{\circ}$)	1.29/0.69 ($^{\circ}$)
$\sigma_{\phi_{E,n_2}^{T/R}} / \sigma_{\phi_{A,n_2}^{T/R}}$	10/6.3 ($^{\circ}$)	0.5/0.6 ($^{\circ}$)

$$\begin{aligned} \bar{\tau}_{pq}(t) &= \sum_{n_1=1}^{N_1^{pq}(t)} \sum_{m_{n_1}=1}^{M_{n_1}} \tilde{P}_{m_{n_1}}^{pq}(t) \tau_{m_{n_1}}^{pq}(t) \\ &+ \sum_{n_2=1}^{N_2^{pq}(t)} \sum_{m_{n_2}=1}^{M_{n_2}} \tilde{P}_{m_{n_2}}^{pq}(t) \tau_{m_{n_2}}^{pq}(t). \end{aligned} \quad (77)$$

IV. RESULTS AND ANALYSIS

In this section, statistical properties of the proposed model are simulated and some simulation results are compared with measurement data to validate the proposed channel model. Because the proposed model mainly considers small-scale fading, the path loss and shadowing are ignored in the simulation. For some general simulation parameters produced by normal distributions, the related means and standard deviations are listed in Table II. Moreover, the wind speed at 19.5 m above sea level is assumed to be 5 m/s in the simulation. In Fig. 5, the normalized time-variant delay PSD for different distances are presented with d_{LoS} denoting the initial LoS distance at $t = 0$ s. Three typical distances are chosen to represent different scenarios. The velocities of Tx and Rx are 5 m/s and 10 m/s to fit the movement of ships, respectively. The channel of short-range communication (initial distance is 212 m) is illustrated in Fig. 5(a). In this case, the clusters are generated because of the fluctuating waves. The change in the moving distance of Tx reflects the evolution of time, and the birth-death process of clusters during this period can be observed. In Fig. 5(b), the distance between Tx and Rx is larger than d_{break} . The influence of evaporation duct leads to more scattering paths. As illustrated in Fig. 5(c), the LoS path is blocked by the curvature of the earth when the distance between Tx and Rx continues to increase, and the number of scattering clusters decreases because sea waves no longer affect the communications. The changes of delay PSDs for channels with different communication distances show that the proposed model can describe the location-dependent characteristic of maritime channels.

The absolute values of the local ACF and CCF of the channel model at different distances are shown in Fig. 6 and Fig. 7, respectively. The curves are obtained using the Monte Carlo method. For each curve, 1000 samples are generated and the curves illustrate the mean values of the samples. The 95% confidence intervals for each curve are given as the translucent regions. There are similar trends in these two statistical characteristics, that the descend rates of ACF and CCF curves decrease with the increasing distances.

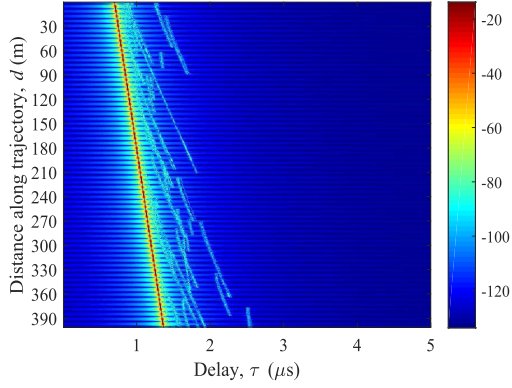
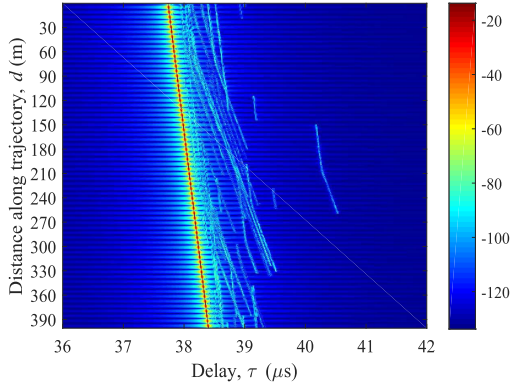
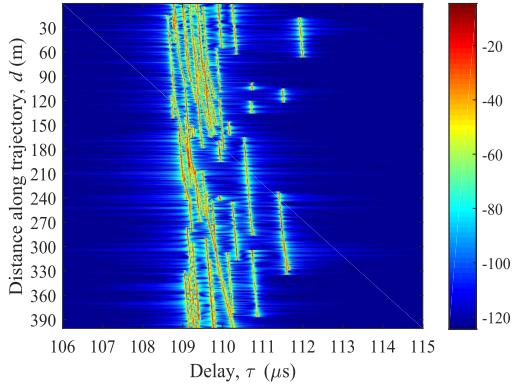
(a) Scenario 1 ($d_{\text{LoS}} = 212$ m).(b) Scenario 2 ($d_{\text{LoS}} = 11312$ m).(c) Scenario 3 ($d_{\text{LoS}} = 32522$ m).

Fig. 5. The normalized time-variant delay PSD of different communication scenarios ($f_c = 5.8$ GHz, $v_R = 5$ m/s, $v_T = 10$ m/s, $\theta_A^T = 5\pi/4$, $\theta_E^T = \pi/3$, $\theta_A^R = \pi/4$, $\theta_E^R = \pi/3$).

Because the angular spread of the scattering paths from duct propagation is smaller than that of the scattering paths from sea surface, the induced phase shifts of duct scattering paths are relatively small which makes the correlations fall more slowly. It is worth noting that the CCF curve of scenario 2 initially declines the fastest, which may be caused by a more dramatic phase shift generated from the superposition of the two kinds of clusters. Fig. 8 illustrates the effects of carrier frequencies and time on temporal ACF in scenario 2. The ACF curves are obtained using the same method as above. The trend changes

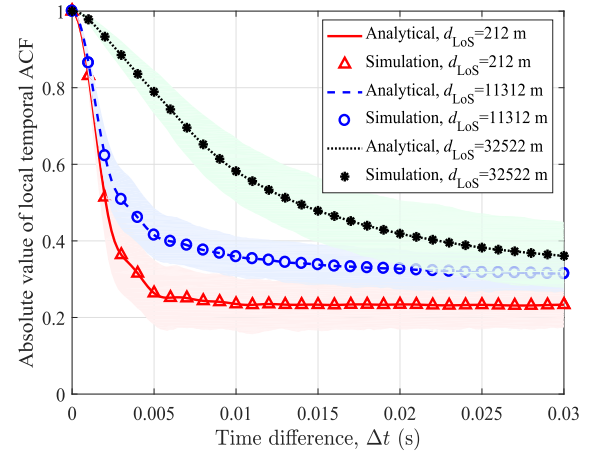


Fig. 6. The analytical and simulated temporal ACFs with 95% confidence intervals in different communication scenarios ($f_c = 5.8$ GHz, $v_R = 5$ m/s, $v_T = 10$ m/s, $\lambda_G = 30$, $\lambda_R = 1$).

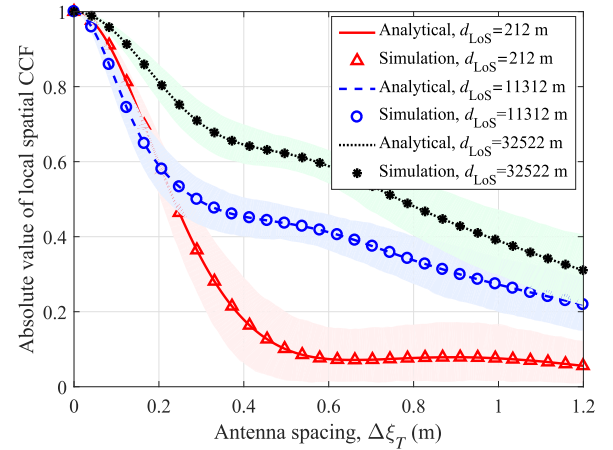


Fig. 7. The analytical and simulated spatial CCFs with 95% confidence intervals in different communication scenarios ($f_c = 5.8$ GHz, $v_R = 5$ m/s, $v_T = 10$ m/s, $\lambda_G = 30$, $\lambda_R = 1$).

of ACFs over time result from the position shift of Tx/Rx and the birth-death process of clusters. It can be observed that higher frequency leads to faster decline in correlation. Moreover, the analytical results generated from the derived theoretical formula and simulation results generated from the correlation calculation of CIR match well, which verifies the validity of the simulations and derivations.

The comparison of stationary interval CDF curves for different scenarios is given in Fig. 9. The three curves are simulated with the same speeds of Tx and Rx to eliminate the influence of speed on the results. From Fig. 9, it can be found that the stationary interval of the scenario 3 is largest, while that of the scenario 1 is smallest. This phenomenon indicates that the channel will change more slowly and become more stationary as the communication distance increases gradually.

In Fig. 10(a) and Fig. 10(b), the power distribution along the AAoD and EAoD axes are provided. The yellow line and its vicinity represent the power of the scattering paths from evaporation duct propagation and mean that their angles are relatively concentrated. Some weak power lines representing

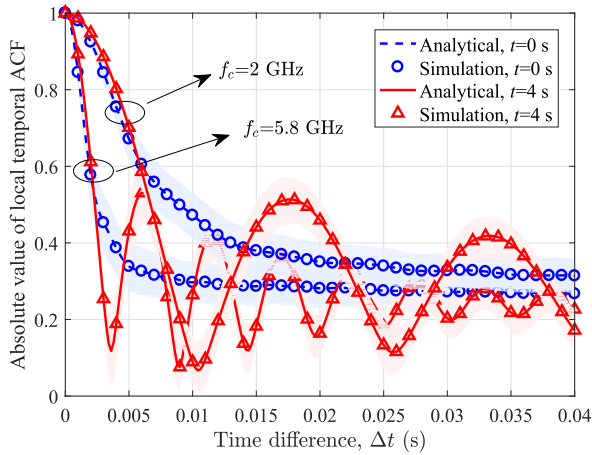


Fig. 8. The temporal ACFs with 95% confidence intervals in scenario 2 at $t = 0$ s and $t = 4$ s ($d_{\text{LoS}} = 11312$ m, $f_c = 5.8$ GHz/2 GHz, $v_R = 5$ m/s, $v_T = 10$ m/s, $\lambda_G = 30$, $\lambda_R = 1$).

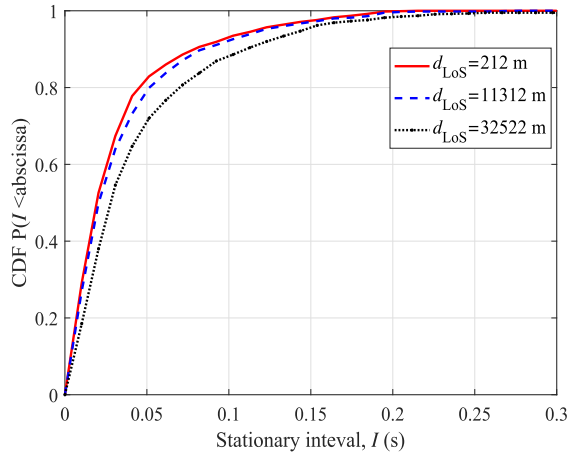
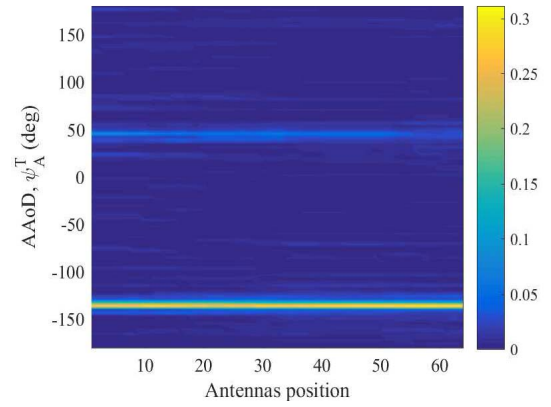


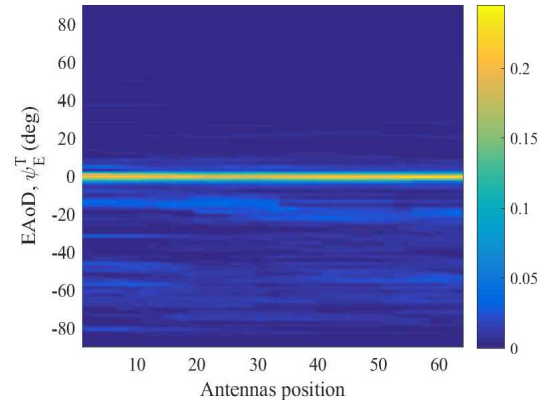
Fig. 9. CDFs of stationary interval in different communication scenarios ($f_c = 5.8$ GHz, $v_R = 5$ m/s, $v_T = 10$ m/s, $\lambda_G = 30$, $\lambda_R = 1$).

the clusters from sea surface are distributed within the given limited range. Here, the Tx with 64 antennas and Rx with 1 antenna are adopted to embody the evolution of clusters on the Tx array. In these two figures, the birth-death process of the clusters in space domain is presented.

The CDF curves of the RMS delay spread of channels at different scenarios are presented in Fig. 11. By comparing the curves, it can be found that the longer the distance, the more dispersive the delay values of the paths in channels. In Fig. 12, the simulation result and measurement data in [48] are compared. The measurement was conducted at 1.9 GHz in a communication link of 40 m–30 km. The same parameters are used in our simulation. The simulation curve is obtained after the average operation of 20 simulation samples. Through the comparison, it can be observed that the simulation curve of the proposed model can fit the measurement result well, which proves the accuracy of the channel model. Besides, the simulation result based on the Rural Macro (RMa) scenario in the 3GPP TR 38.901 channel model [30] is provided for reference. To compare the similarity between the delay spread distributions of different models and the measurement data, the Kolmogorov-Smirnov (K-S) test statistics are calculated. The



(a) The angular PSD of AAoD.



(b) The angular PSD of EAoD.

Fig. 10. The angular PSD of AAoD and EAoD at Tx side ($f_c = 5.8$ GHz, $v_R = 5$ m/s, $v_T = 10$ m/s, $\theta_A^T = \pi/4$, $\theta_E^T = \pi/3$, $\theta_A^R = \pi/4$, $\theta_E^R = \pi/3$).

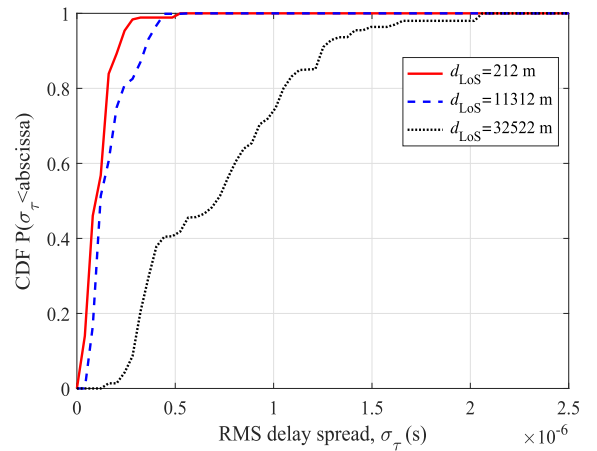


Fig. 11. CDFs of RMS delay spread in different communication scenarios ($f_c = 5.8$ GHz, $v_R = 5$ m/s, $v_T = 10$ m/s, $\theta_A^T = \pi/3$, $\theta_E^T = \pi/4$, $\theta_A^R = \pi/4$, $\theta_E^R = \pi/4$).

K-S test statistic between the land-based 3GPP channel model and the measurement data is 0.9205, while the K-S test statistic between the proposed channel model and the measurement data is 0.1701. The smaller K-S test statistic indicates that the proposed channel model can better describe the distribution of delay spread for the maritime scenarios.

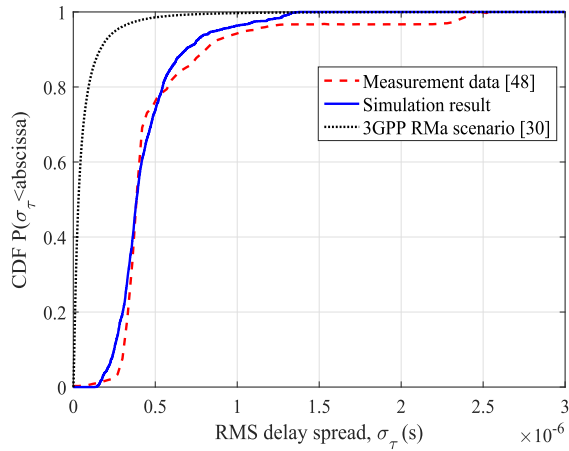


Fig. 12. CDFs of RMS delay spread of the proposed channel model, 3GPP TR38.901 RMa scenario [30], and measurement data in [48] ($f_c = 1.9$ GHz, $v_R = 10$ m/s, $v_T = 10$ m/s, $\theta_A^T = \pi/3$, $\theta_E^T = \pi/4$, $\theta_A^R = \pi/4$, $\theta_E^R = \pi/4$).

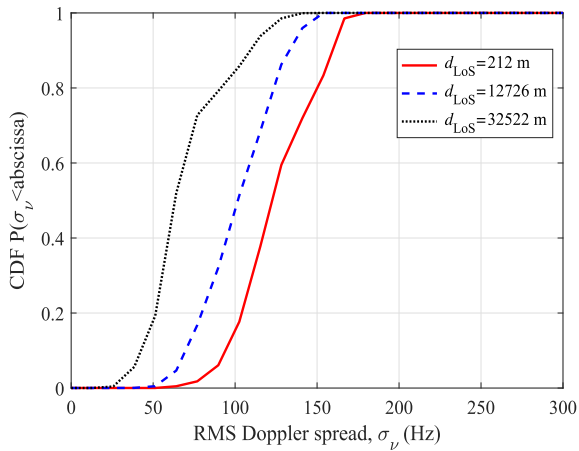


Fig. 13. CDFs of RMS Doppler spread in different communication scenarios ($f_c = 5.8$ GHz, $v_R = 5$ m/s, $v_T = 10$ m/s, $\theta_A^T = \pi/3$, $\theta_E^T = \pi/4$, $\theta_A^R = \pi/4$, $\theta_E^R = \pi/4$).

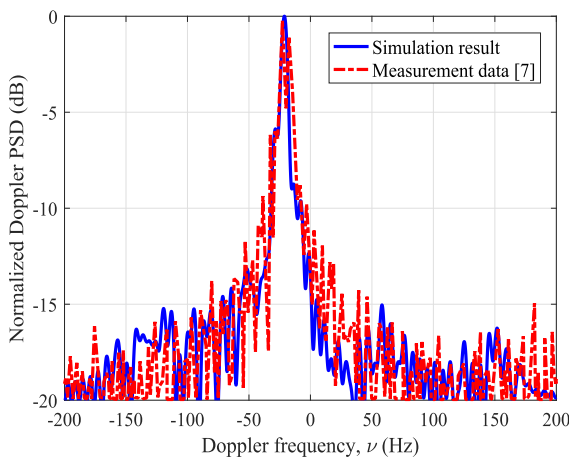


Fig. 14. Normalized Doppler PSD of proposed channel model and measurement data in [7] ($f_c = 5.2$ GHz, $v_R = 7$ m/s, $v_T = 7$ m/s, $\theta_A^T = \pi/3$, $\theta_E^T = \pi/4$, $\theta_A^R = \pi/4$, $\theta_E^R = \pi/4$).

Fig. 13 gives the CDF curves of the RMS Doppler spread. The difference between the curves illustrates that the value range of RMS Doppler spread shrinks as the distance increases, which is contrary to the trend of RMS delay spread.

Fig. 14 provides the normalized Doppler PSD and compares it with the measurement data [7]. The channel measurement was carried out in a scene where two ships were driving towards each other. During the measurement, the carrier frequency was 5.2 GHz and the ships' speeds were between 2 m/s and 7 m/s. In the simulation, the speed 7 m/s is used. Because the Doppler PSD was obtained when both ships were passing each other (fitted into scenario 1), the Doppler frequency shift of LoS path was close to 0 Hz. The good consistency between the simulation result and measurement data validates the utility of the proposed channel model to simulate the actual maritime communication scenario.

V. CONCLUSION

In this paper, we have proposed a 3D non-stationary MIMO GBSM for ship-to-ship maritime communication channels. Through taking into account the influence of sea surface fluctuation and evaporation duct propagation on scatterer distribution, the model can achieve long-distance multi-scenario simulation, and the channel structures are location-dependent. The movements of Tx/Rx, the variations of environment factors, and the effect of massive MIMO arrays have been characterized by the time-variant channel parameters and the birth-death process of clusters on the array and time domains to reflect the spatial and temporal non-stationary properties of the channel. Statistical properties like delay PSD, stationary interval, STCF, angular PSD, Doppler PSD, and RMS delay/Doppler spreads have been derived, and the simulation curves in different scenarios have been compared. The correctness of the derivation has been validated by the consistency of the theoretical results and simulation results. The comparisons of simulated RMS delay spread and Doppler PSD with corresponding channel measurement results have verified the practicality of the proposed model. For the future work, the proposed channel model will be extended to support the long-distance communication channel between ships and satellites, and the influences of ship tilting and shaking will be studied.

REFERENCES

- [1] J. Wang *et al.*, "Wireless channel models for maritime communications," *IEEE Access*, vol. 6, pp. 68070–68088, Nov. 2018.
- [2] Y. He, H. Chang, Y. Liu, W. Zhang, J. Sun, and C.-X. Wang, "A 3D GBSM for ship-to-land communications," in *Proc. IEEE/CIC ICC*, Changchun, China, Aug. 2019, pp. 967–972.
- [3] C.-X. Wang, J. Huang, H. Wang, X. Gao, X. You, and Y. Hao, "6G wireless channel measurements and models: Trends and challenges," *IEEE Veh. Technol. Mag.*, vol. 15, no. 4, pp. 22–32, Dec. 2020.
- [4] X. You *et al.*, "Towards 6G wireless communication networks: Vision, enabling technologies, and new paradigm shifts," *Sci. China Inf. Sci.*, vol. 64, no. 1, pp. 1–74, Jan. 2021, doi: 10.1007/s11432-020-2955-6.
- [5] C.-X. Wang, J. Bian, J. Sun, W. Zhang, and M. Zhang, "A survey of 5G channel measurements and models," *IEEE Commun. Surveys Tuts.*, vol. 20, no. 4, pp. 3142–3168, 4th Quart., 2018.
- [6] W. Wang *et al.*, "Propagation channel at 5.2 GHz in Baltic Sea with focus on scattering phenomena," in *Proc. 9th Eur. Conf. Antennas Propag. (EuCAP)*, Lisbon, Portugal, Apr. 2015, pp. 1–5.
- [7] W. Wang, T. Jost, R. Raulefs, and U. Fiebig, "Ship-to-ship broadband channel measurement at 5.2 GHz on North sea," in *Proc. EuCAP*, Paris, France, May 2017, pp. 3872–3876.
- [8] W. Wang, R. Raulefs, and T. Jost, "Fading characteristics of maritime propagation channel for beyond geometrical horizon communications in C-band," *CEAS Space J.*, vol. 9, pp. 1–10, Dec. 2017.

- [9] J. C. Reyes-Guerrero, "Experimental broadband channel characterization in a sea port environment at 5.8 GHz," *IEEE J. Ocean. Eng.*, vol. 41, no. 3, pp. 509–514, Jul. 2016.
- [10] J. C. Reyes-Guerrero and L. A. Mariscal, "Experimental time dispersion parameters of wireless channels over sea at 5.8 GHz," in *Proc. ELMAR*, Zadar, Croatia, Sep. 2012, pp. 89–92.
- [11] J. Joe *et al.*, "Path loss measurements in sea port for WiMAX," in *Proc. WCNC*, Kowloon, China, Jun. 2007, pp. 1871–1876.
- [12] J. Lee, J. Choi, J. Lee, and S. Kim, "Experimental results of a land-to-ship propagation channel using a wideband channel sounding system at 2.4 GHz," in *Proc. ICNC*, Maui, HI, USA, Mar. 2018, pp. 243–248.
- [13] F. Dong and Y. H. Lee, "Experiment results of a two-by-two diverse antenna system over sea surface in NLOS scenario," in *Proc. ISAP*, Chicago, IL, USA, Jul. 2012, pp. 1–2.
- [14] K. Yang, T. Røste, F. Bekkadal, and T. Ekman, "Experimental multipath delay profile of mobile radio channels over sea at 2 GHz," in *Proc. LAP* Loughborough, U.K., Nov. 2012, pp. 1–4.
- [15] T. Røste, K. Yang, and F. Bekkadal, "Coastal coverage for maritime broadband communications," in *Proc. IEEE OCEANS'13-Bergen*, Bergen, Norway, Jun. 2013, pp. 1–8.
- [16] Q. Zhang, K. Yang, Y. Shi, and X. Yan, "Oceanic propagation measurement in the Northern part of the South China Sea," in *Proc. IEEE OCEANS*, Shanghai, China, Apr. 2016, pp. 1–4.
- [17] Y. H. Lee, F. Dong, and Y. S. Meng, "Near sea-surface mobile radiowave propagation at 5 GHz: Measurements and modelling," *Radioengineering*, vol. 23, no. 3, pp. 824–830, Sep. 2014.
- [18] Y. H. Lee and Y. S. Meng, "Key considerations in the modeling of tropical maritime microwave attenuations," *Int. J. Antennas Propag.*, vol. 2015, no. 4, pp. 1–7, Mar. 2015.
- [19] N. Mehrnia and M. K. Ozdemir, "Novel maritime channel models for millimeter radiowaves," in *Proc. SoftCOM*, Split, Croatia, Sep. 2016, pp. 1–6.
- [20] N. Mehrnia and M. K. Ozdemir, "Multipath delay profile and Doppler spread of millimeter radiowaves over the sea channel," in *Proc. IEEE BlackSeaCom*, Istanbul, Turkey, Jun. 2017, pp. 1–5.
- [21] J. Mansukhani and S. Chakrabarti, "Small scale characterization of marine channel using the finite-difference time domain method," in *Proc. ICCNT*, Coimbatore, India, Jul. 2012, pp. 1–7.
- [22] I. J. Timmins and S. O'Young, "Marine communications channel modeling using the finite-difference time domain method," *IEEE Trans. Veh. Technol.*, vol. 58, no. 6, pp. 2626–2637, Jul. 2009.
- [23] K. Yang, T. Ekman, T. Røste, and F. Bekkadal, "A quasi-deterministic path loss propagation model for the open sea environment," in *Proc. WPMC*, Brest, France, Oct. 2011, pp. 1–5.
- [24] W. Wang, T. Jost, and R. Raulefs, "A semi-deterministic path loss model for in-harbor LoS and NLoS environment," *IEEE Trans. Antennas Propag.*, vol. 65, no. 12, pp. 7399–7404, Dec. 2017.
- [25] J. Wang, Y. Cui, S. Ma, X. Meng, and J. Teng, "A simulation model for ship-to-ship Rayleigh fading channels," in *Proc. ICSP*, Hangzhou, China, Oct. 2014, pp. 1692–1697.
- [26] J. Wang, Y. Cui, S. Ma, X. Meng, L. Liu, and J. Teng, "A non-isotropic simulation model for ship-to-ship fading channels," in *Proc. ICWMMN*, Beijing, China, Nov. 2015, pp. 115–119.
- [27] G. Dahman, D. Couillard, M.-E. Grandmaison, G. Poitou, and F. Gagnon, "Improved 2-Ray model for overwater propagation channels: Modeling the instantaneous variations in the received signal strength," *IEEE Wireless Commun. Lett.*, vol. 8, no. 3, pp. 865–868, Jun. 2019.
- [28] W. J. Pierson and L. Moskowitz, "A proposed spectral form for fully developed wind seas based on the similarity theory of S. A. Kitaigorodskii," *J. Geophys. Res. Atmos.*, vol. 69, no. 24, pp. 5181–5190, Dec. 1964.
- [29] R. Verdone and A. Zanella, *Pervasive Mobile Ambient Wireless Communication*. London, U.K.: Springer, 2012.
- [30] *Study on Channel Model for Frequencies From 0.5 to 100 GHz*, document TR 38.901, V14.0.0, 3GPP, Mar. 2017.
- [31] W. J. Pierson, "The theory and applications of ocean wave measuring systems at and below the sea surface, on the land, from aircraft, and from spacecraft," NASA, Washington, DC, USA, Tech. Rep. NASA-CR-2646, Jan. 1976.
- [32] P. Kyösti, *WINNER II channel models*, document IST-4-027756, WINNER II D1.1.2, V1.2, Apr. 2008.
- [33] J. Meinila *et al.*, *WINNER+Final Channel Models*, document CELTIC/CP5-026, WINNER+ D5.3 v1.0, Jun. 2010.
- [34] H. Chang *et al.*, "A novel nonstationary 6G UAV-to-ground wireless channel model with 3-D arbitrary trajectory changes," *IEEE Internet Things J.*, vol. 8, no. 12, pp. 9865–9877, Jun. 2021.
- [35] E. Dinc and O. B. Akan, "Channel model for the surface ducts: Large-scale path-loss, delay spread, and AOA," *IEEE Trans. Antennas Propag.*, vol. 63, no. 6, pp. 2728–2738, Jun. 2015.
- [36] R. A. Paulus, "Evaporation duct effects on sea clutter," *IEEE Trans. Antennas Propag.*, vol. 38, no. 11, pp. 1765–1771, Nov. 1990.
- [37] N. L. Johnson and S. Kotz, *Continuous Univariate Distributions*. Boston, MA, USA: Houghton Mifflin, 1970.
- [38] Y. Karasawa and T. Shiokawa, "Characteristics of L-band multipath fading due to sea surface reflection," *IEEE Trans. Antennas Propag.*, vol. AP-32, no. 6, pp. 618–623, Jun. 1984.
- [39] T. Elfouhaily, B. Chapron, K. Katsaros, and D. Vandemark, "A unified directional spectrum for long and short wind-driven waves," *J. Geophys. Res., Ocean.*, vol. 102, no. 7, pp. 15781–15796, Jul. 1997.
- [40] S. C. Wen, D. Zhang, B. Chen, and P. Guo, "Theoretical wind wave frequency spectra in deep water – I. Form of spectrum," *Acta Oceanologica Sinica*, vol. 7, no. 1, pp. 6–21, Jun. 1988.
- [41] S. Wu, C.-X. Wang, E.-H.-M. Aggoune, M. M. Alwakeel, and X. You, "A general 3-D non-stationary 5G wireless channel model," *IEEE Trans. Commun.*, vol. 66, no. 7, pp. 3065–3078, Jul. 2018.
- [42] J. Bian, C.-X. Wang, X. Gao, X. You, and M. Zhang, "A general 3D non-stationary wireless channel model for 5G and beyond," *IEEE Trans. Wireless Commun.*, vol. 20, no. 5, pp. 3211–3224, May 2021.
- [43] T. Zwick, C. Fischer, D. Didascalou, and W. Wiesbeck, "A stochastic spatial channel model based on wave-propagation modeling," *IEEE J. Sel. Areas Commun.*, vol. 18, no. 1, pp. 6–15, Jan. 2000.
- [44] H. Iwai and Y. Karasawa, "Wideband propagation model for the analysis of the effect of the multipath fading on the near-far problem in CDMA mobile radio systems," *IEICE Trans. Commun.*, vol. 76B, no. 2, pp. 103–112, Feb. 1993.
- [45] B. Chen, Z. Zhong, and B. Ai, "Stationarity intervals of time-variant channel in high speed railway scenario," *China Commun.*, vol. 9, no. 8, pp. 64–70, Aug. 2012.
- [46] Y. Liu, C.-X. Wang, J. Huang, J. Sun, and W. Zhang, "Novel 3-D non-stationary mmWave massive MIMO channel models for 5G high-speed train wireless communications," *IEEE Trans. Veh. Technol.*, vol. 68, no. 3, pp. 2077–2086, Mar. 2019.
- [47] B. Boashash, "Estimating and interpreting the instantaneous frequency of a signal. I. Fundamentals," *Proc. IEEE*, vol. 80, no. 4, pp. 520–538, Apr. 1992.
- [48] K. Maliatsos, P. Loulis, M. Chronopoulos, P. Constantinou, P. Dallas, and M. Ikonou, "Experimental small scale fading results for mobile channels over the sea," in *Proc. IEEE 17th Int. Symp. Pers., Indoor Mobile Radio Commun.*, Helsinki, Finland, Sep. 2006, pp. 1–5.



Yubei He received the B.Sc. degree from the School of Information Science and Engineering, Shandong University, Qingdao, China, in 2017, where she is currently pursuing the Ph.D. degree in information and communication engineering. Her current research interests include maritime communications, wireless propagation channel measurements and channel modeling, and B5G/6G wireless communications.



Cheng-Xiang Wang (Fellow, IEEE) received the B.Sc. and M.Eng. degrees in communication and information systems from Shandong University, China, in 1997 and 2000, respectively, and the Ph.D. degree in wireless communications from Aalborg University, Denmark, in 2004.

He was a Research Assistant with the Hamburg University of Technology, Hamburg, Germany, from 2000 to 2001, a Visiting Researcher with Siemens AG Mobile Phones, Munich, Germany, in 2004, and a Research Fellow with the University of Agder, Grimstad, Norway, from 2001 to 2005. He has been with Heriot-Watt University, Edinburgh, U.K., since 2005, where he was promoted as a Professor in 2011. In 2018, he joined Southeast University, Nanjing, China, as a Professor. He is also a part-time Professor with Purple Mountain Laboratories, Nanjing. He has authored four books, three book chapters, and more than 440 papers in refereed journals and conference proceedings, including 25 highly cited papers. He has also delivered 22 invited keynote speeches/talks and nine tutorials in international conferences. His current research interests include wireless channel measurements and modeling, 6G wireless communication networks, and applying artificial intelligence to wireless communication networks.

Dr. Wang is a member of the Academia Europaea (The Academy of Europe), a fellow of IET and the China Institute of Communication (CIC), an IEEE Communications Society Distinguished Lecturer in 2019 and 2020, and a Highly-Cited Researcher recognized by Clarivate Analytics from 2017 to 2020. He is currently an Executive Editorial Committee Member of the IEEE TRANSACTIONS ON WIRELESS COMMUNICATIONS. He has served as an Editor for nine international journals, including the IEEE TRANSACTIONS ON WIRELESS COMMUNICATIONS from 2007 to 2009, the IEEE TRANSACTIONS ON VEHICULAR TECHNOLOGY from 2011 to 2017, and the IEEE TRANSACTIONS ON COMMUNICATIONS from 2015 to 2017. He was a Guest Editor of the IEEE JOURNAL ON SELECTED AREAS IN COMMUNICATIONS, Special Issue on Vehicular Communications and Networks (Lead Guest Editor), Special Issue on Spectrum and Energy Efficient Design of Wireless Communication Networks, and Special Issue on Airborne Communication Networks. He was also a Guest Editor for the IEEE TRANSACTIONS ON BIG DATA, Special Issue on Wireless Big Data, and is a Guest Editor for the IEEE TRANSACTIONS ON COGNITIVE COMMUNICATIONS AND NETWORKING, Special Issue on Intelligent Resource Management for 5G and Beyond. He has served as a TPC member, the TPC chair, and the general chair for more than 80 international conferences. He received the 14 Best Paper Awards from IEEE GLOBECOM 2010, IEEE ICCT 2011, ITST 2012, IEEE VTC 2013-Spring, IWCMC 2015, IWCMC 2016, IEEE/CIC ICC 2016, WPMC 2016, WOCC 2019, IWCMC 2020, WCSP 2020, CSPS2021, and WCSP 2021. Also, he received the 2020 and 2021 "AI 2000 Most Influential Scholar Award Honourable Mention" in recognition of his outstanding and vibrant contributions in the field of the Internet of Things.



Hengtai Chang received the B.Sc. and Ph.D. degrees from the School of Information Science and Engineering, Shandong University, China, in 2016 and 2021, respectively. He is currently a Post-Doctoral Research Associate at Purple Mountain Laboratories, China, and a Post-Doctoral Research Associate at the China National Mobile Communications Research Laboratory, Southeast University, China. His current research interests include UAV communications, wireless propagation channel measurements and channel modeling, and B5G/6G wireless communications.



Jie Huang (Member, IEEE) received the B.E. degree in information engineering from Xidian University, China, in 2013, and the Ph.D. degree in information and communication engineering from Shandong University, China, in 2018. From October 2018 to October 2020, he was a Post-Doctoral Research Associate at the National Mobile Communications Research Laboratory, Southeast University, China, supported by the National Post-Doctoral Program for Innovative Talents. From January 2019 to February 2020, he was a Post-Doctoral Research Associate at Durham University, U.K. Since March 2019, he has been a part-time Researcher at Purple Mountain Laboratories, China. Since November 2020, he has been an Associate Professor with the National Mobile Communications Research Laboratory, Southeast University. He has authored and coauthored more than 40 papers in refereed journals and conference proceedings. His research interests include millimeter wave, massive MIMO, reconfigurable intelligent surface channel measurements and modeling, wireless big data, and 6G wireless communications. He received the Best Paper Awards from WPMC 2016, WCSP 2020, and WCSP 2021. He has served as a TPC Member for IEEE/CIC ICC 2017, 2018, and 2021, and delivered two tutorials in IEEE/CIC 2021 and IEEE PIMRC 2021.



Jian Sun (Member, IEEE) received the B.Sc. degree in applied electronic technology, the M.Eng. degree in measuring and testing technologies and instruments, and the Ph.D. degree in communication and information systems from Zhejiang University, Hangzhou, China, in 1996, 1999, and 2005, respectively. From 2005 to 2018, he was a Lecturer with the School of Information Science and Engineering, Shandong University, China. Since 2018, he has been an Associate Professor. In 2008, he was a Visiting Scholar with the University of California San Diego (UCSD). In 2011, he was a Visiting Scholar with Heriot-Watt University, U.K., supported by U.K.–China Science Bridges: Research and Development on (B)4G Wireless Mobile Communications Project. His current research interests include signal processing for wireless communications, channel sounding and modeling, joint communications and sensing, maritime communication, visible light communication, and software defined radio.



Wensheng Zhang (Member, IEEE) received the M.E. degree in electrical engineering from Shandong University, China, in 2005, and the Ph.D. degree in electrical engineering from Keio University, Japan, in 2011. In 2011, he joined the School of Information Science and Engineering, Shandong University, where he is currently an Associate Professor. He was a Visiting Scholar at the University of Oulu, Finland, in 2010, and the University of Arkansas, USA, 2019. His research interests lie in tensor computing, random matrix theory, and intelligent B5G wireless communications.



El-Hadi M. Aggoune (Life Senior Member, IEEE) received the M.S. and Ph.D. degrees in electrical engineering from the University of Washington (UW), Seattle, WA, USA. He taught graduate and undergraduate courses in electrical engineering at many universities in the USA and abroad. He served at many academic ranks, including an Endowed Chair Professor. He is listed as an Inventor in two patents assigned to the Boeing Company, USA, and the Sensor Networks and Cellular Systems Research Center, the University of Tabuk, Saudi Arabia. He is also a Professional Engineer registered in Washington. He is currently serving as a Professor and the Director of the SNCS Research Center, University of Tabuk. His research is referred to in many patents, including patents assigned to ABB, Switzerland, and EPRI, USA. He has authored many papers in IEEE and other journals and conferences. His research interests include wireless sensor networks, energy systems, and scientific visualization. He is serving on many technical committees for conferences worldwide and a reviewer for many journals. One of his Laboratories received the Boeing Supplier Excellence Award. He was the recipient of the IEEE Professor of the Year Award, UW Branch.